Ore Geology Reviews 86 (2017) 807–824

Contents lists available at ScienceDirect

Ore Geology Reviews

journal homepage: www.elsevier.com/locate/oregeo

Zircon and molybdenite geochronology and geochemistry of the Kalmakyr porphyry Cu–Au deposit, Almalyk district, Uzbekistan: Implications for mineralization processes

Xiao-Bo Zhao [a], Chun-Ji Xue [a,*], Guo-Xiang Chi [b], Xuan-Xue Mo [a], Bakhtiar Nurtaev [c], Guo-Zhen Zhang [a]

[a] State Key Laboratory of Geological Processes and Mineral Resources, School of Earth Sciences and Resources, China University of Geosciences, Beijing 100083, China
[b] Department of Geology, University of Regina, Regina S4S 0A2, Canada
[c] Institute of Geology and Geophysics, Academy of Sciences of Uzbekistan, Tashkent 100041, Uzbekistan

ARTICLE INFO

Article history:
Received 7 October 2016
Received in revised form 14 March 2017
Accepted 6 April 2017
Available online 8 April 2017

Keywords:
Late Carboniferous
Porphyry Cu–Au–Mo mineralization
Kalmakyr
Turkestan Ocean
Tien Shan

ABSTRACT

Copper, gold and molybdenum mineralization of the Kalmakyr porphyry deposit in Uzbek Tien Shan occurs as stockworks, veinlets and disseminations in the phyllic and K-silicate alteration zones developed predominantly in a middle to late Carboniferous intrusive complex composed of monzonite and granodiorite porphyry. Zircon U–Pb dating yielded an age of 327.2 ± 5.6 Ma for the ore-hosting monzonite and an age of 313.6 ± 2.8 Ma for the ore-bearing granodiorite porphyry. Re–Os dating of seven molybdenite samples from stockwork and veinlet ores yielded model ages from 313.2 to 306.3 Ma, with two well-constrained isochron ages of 307.6 ± 2.5 Ma (five stockwork ores) and 309.1 ± 2.2 Ma (five stockwork ores and two veinlet ores), respectively. These results indicate that Cu–Au mineralization post-dated the emplacement of the monzonite, started right after the emplacement of the granodiorite porphyry, and lasted for ca. 7 Ma afterward. The geochronological and geochemical data suggest that the Kalmakyr deposit was formed in a late Carboniferous mature magmatic arc setting, probably related to the latest subduction process of the Turkestan Ocean beneath the Middle Tien Shan. The $\varepsilon_{Hf}(t)$ values of zircon grains from the monzonite vary from +11 to +1.7, with an average of +5.1, and those of zircon grains from the granodiorite porphyry range from +5.7 to −1.8, with an average of +2.4. These data indicate that the magma of both monzonite and granodiorite porphyry was derived from partial melting of a thickened lower crust with input of mantle components and variable crustal contamination, and that there was more mantle contribution to the formation of the monzonite than the granodiorite porphyry. The high rhenium concentrations of molybdenite (98–899 ppm) also indicate major mantle contribution of rhenium and by inference ore metals. The relatively high Eu_N/Eu_N^* values (average 0.68), Ce^{4+}/Ce^3 values (average 890) and Ce/Nd values (average 36.8) for zircon grains from the granodiorite porphyry than those from the monzonite (average Eu_N/Eu_N^* = 0.33, average Ce^{4+}/Ce^3 = 624, average Ce/Nd = 3.9) suggest that the magma for the syn-mineralization granodiorite porphyry has higher oxygen fugacity than that for the pre-mineralization monzonite. Based on these data, it is proposed that while the monzonite was emplaced, the oxygen fugacity and volatile contents in the magma were relatively low, and ore metals might disperse in the intrusive rock, whereas when the granodiorite porphyry was emplaced, the oxygen fugacity and volatile contents in the magma were increased, favoring copper and gold enrichment in the magmatic fluids. The Kalmakyr deposit formed from a long-lived magmatic-hydrothermal system connected with fertile magmatic sources in relation to the subduction of the Turkestan Ocean beneath the Middle Tien Shan.

© 2017 Elsevier B.V. All rights reserved.

1. Introduction

The Kalmakyr porphyry Cu–Au–Mo deposit is located in the Almalyk Cu–Au–polymetallic district, about 45 km southeast of Tashkent, the capital city of Uzbekistan (Fig. 1). Measured and indicated resources are approximately 2000 million tons (Mt) of ores grading 0.4% Cu, 0.6 g/t Au, and 0.006% Mo, using a 0.2% Cu

* Corresponding author at: State Key Laboratory of Geological Processes and Mineral, Resources, China University of Geosciences, 29# Xue-Yuan Road, Haidian District, Beijing 100083, China.
E-mail address: chunji.xue@cugb.edu.cn (C.-J. Xue).

http://dx.doi.org/10.1016/j.oregeorev.2017.04.008
0169-1368/© 2017 Elsevier B.V. All rights reserved.

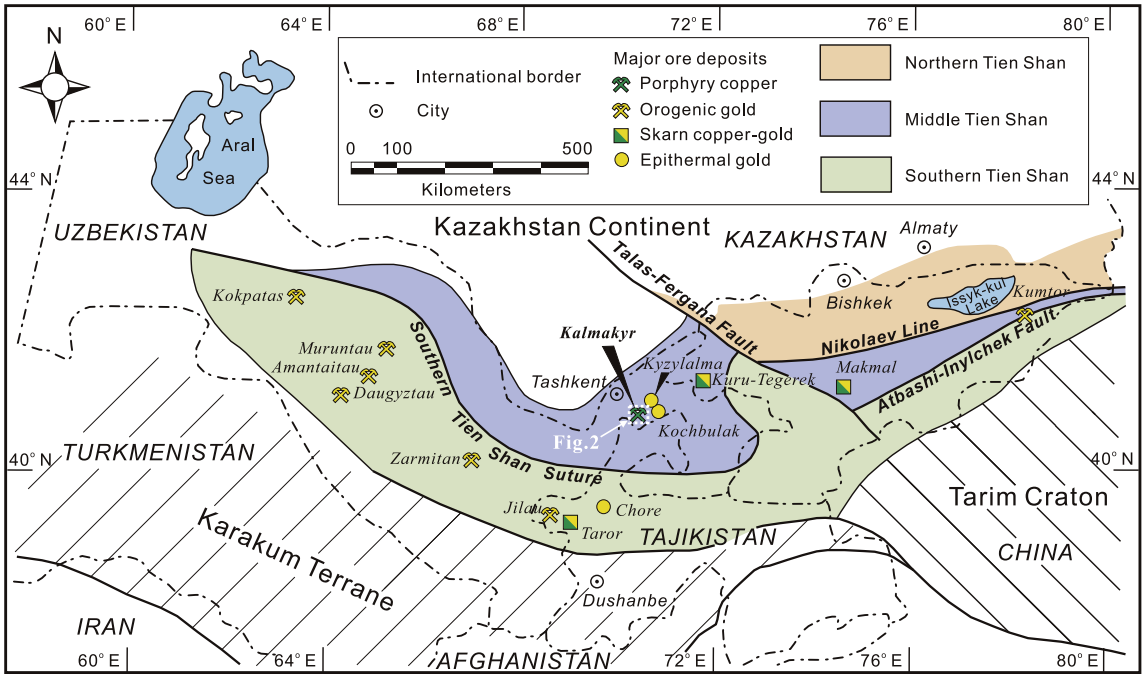

Fig. 1. Simplified geological map of the western section of the Tien Shan orogenic belt showing location of major copper and gold deposits of different styles (modified from Porter (2006)). Area shown in Fig. 2 is marked.

cut-off grade, plus about 1700 Mt of low-grade resources at 0.15–0.19% Cu (Golovanov et al., 2005). The deposit also contains additional inferred resources of 17 t Pd at 0.06 g/t, and 1.7 t Pt at 0.006 g/t (Pašava et al., 2010). Notably, the Kalmakyr deposit has the second largest copper endowment among all deposits in Eurasia, and ranks as the third largest gold endowment of any porphyry copper deposits in the world (Cooke et al., 2005; Mao et al., 2014; Seltmann et al., 2014a; Yakubchuk et al., 2012).

The Kalmakyr deposit is the largest porphyry Cu–Au deposit so far discovered in the 2500-km-long Tien Shan orogenic belt, which extends across Uzbekistan, Tajikistan, Kyrgyzstan, and southeast Kazakhstan into China (Fig. 1). Understanding its tectonomagmatic setting and mineralization processes, including the source and age of the parental magma and the age of mineralization, will be valuable in expanding our knowledge on porphyry mineralization systems in ancient orogenic belts, and also in developing exploration strategies in this highly prospective underexplored region (Zhao et al., 2014a,b).

Porphyry Cu–Au–Mo of the Kalmakyr deposit is associated dominantly with multiple subduction-related alkalic, felsic to intermediate intrusions formed in the Late Carboniferous (Golovanov et al., 2005). Published K–Ar dating has yielded 320–280 Ma ages for magmatic intrusions and 294–273 Ma ages for associated hydrothermal alteration (Golovanov et al., 2005). Previous zircon U–Pb ages for ore-related intrusions (315 ~ 308 Ma; Seltmann et al., 2011) even seems to be contradictory with the intrusive relations by geological mapping. The age of porphyry Cu–Au–Mo mineralization is estimated at 314 Ma based on statistical analyses of the U–Pb ages and assumption that magmatic emplacement age is close to the mineralization age (Seltmann et al., 2011). The estimated age is in agreement with the preliminary Re–Os molybdenite age (314 Ma) reported in Seltmann et al. (2014b). However, poor description of the dated samples and lacking in analytical error makes the age of mineralization not well constrained.

This paper presents new molybdenite Re–Os geochronological data from the Kalmakyr deposit, rare earth element composition as well as U–Pb and Lu–Hf isotopes of zircon grains from ore-related intrusions. These data are used to constrain the source and history of ore-related magmatism and related mineralization, thus providing new insights into the formation processes of the Kalmakyr porphyry Cu–Au deposit and its controlling factors.

2. Regional geological background

The Tien Shan orogen formed during late Paleozoic collision between the early Paleozoic Kazakhstan continent in the north and the Precambrian Karakum terrane and Tarim craton in the south (Fig. 1) (Biske and Seltmann, 2010; Han et al., 2011; Windley et al., 2007; Yakubchuk et al., 2002), and it is part of the larger Central Asian Orogenic Belt (Jahn et al., 2000; Sengör et al., 1993; Windley et al., 2007; Xiao et al., 2013). The western part of the Tien Shan in Uzbekistan and Kyrgyzstan has generally been subdivided into the Northern, Middle, and Southern Tien Shan, which are bounded by major sutures and crustal-scale faults (Fig. 1).

The Northern Tien Shan consists of Precambrian basement and overlying early Paleozoic continental magmatic rocks formed in response to the progressive northward subduction of the Terskey Ocean beneath the Northern Tien Shan in the Late Ordovician, and to the accretion of Middle Tien Shan to Northern Tien Shan (Konopelko et al., 2008, 2012; Zhao et al., 2015, 2017). In Kyrgyzstan, the Northern Tien Shan is separated from the Middle Tien Shan by the Nikolaev Line (Fig. 1), a late Paleozoic strike-slip fault generally following the early Paleozoic suture zone (Bakirov et al., 2003; Konopelko et al., 2012; Lomize et al., 1997).

The Middle Tien Shan west of the Talas-Fergana fault is represented by the late Paleozoic Beltau–Kurama volcano-plutonic arc belt formed on Precambrian basement, early Paleozoic shallow and deep marine sedimentary sequences and middle Paleozoic arc-related magmatic rocks as a result of the northward subduction of the Turkestan Ocean (Chernyshev et al., 2011; Seltmann et al., 2011). The Beltau–Kurama belt is thought to be a southern

active continental margin of the Kazakhstan continent (Biske and Seltmann, 2010; Golovanov et al., 2005; Yakubchuk et al., 2002), and is characterized by two major episodes of subduction-related magmatism in Silurian–Early Devonian and Late Carboniferous, separated by amagmatic event represented by Middle Devonian to Early Carboniferous carbonate sequences. The younger magmatic episode continued until the Permian. It is genetically associated with major porphyry Cu–Au–Mo deposits in the Almalyk district (e.g. Kalmakyr, Dalnee and Sari-Cheku).

The Southern Tien Shan is an intensely deformed late Paleozoic thrust-and-fold belt that formed during the final closure of the Turkestan Ocean in the Early Permian (Biske and Seltmann, 2010). It is separated from the Middle Tien Shan by the ophiolite-bearing Turkestan Suture in Uzbekistan and the Atbashi-Inylchek Fault in Kyrgyzstan (Fig. 1) (Biske and Seltmann, 2010; Konopelko et al., 2007; Seltmann et al., 2011; Yakubchuk et al., 2002).

3. Geology of the Almalyk district

The Almalyk district is situated on the northern side of the Kurama range (Fig. 1). The district hosts four major porphyry Cu–Au deposits, one skarn Zn–Pb deposit and several important epithermal Au deposits (Fig. 2) with combined historical production and remaining resources of over 21 Mt copper and 2000 t gold on both sides of the Uzbekistan-Tajikistan border (Seltmann et al., 2011). The basal sequence exposed in the Almalyk district is the Ordovician to Lower Silurian shallow marine formations of sandstone and mudstone that were locally greenschist facies metamorphosed. This marine sequence is overlain unconformably by the Lower Devonian intermediate to felsic volcano-sedimentary rocks with zircon U–Pb age of 421 ± 4 Ma (Nurtaev B.S., pers. comm.). Shallow lagoon facies sedimentation in the Middle Devonian to Early Carboniferous resulted in a deposition of approximately 1000 m thick clastic and carbonate succession, with gypsum and anhydrite occurring at the bottom of this package (Shayakubov et al., 1999). The Upper Carboniferous alkaline-rich felsic and intermediate volcanic and associated clastic formation hosts important epithermal gold mineralization in this region (Fig. 2). The overlying Permian unit mainly comprises terrigenous mafic to intermediate volcanic rocks with interbedded conglomerate, siltstone and sandstone. Cretaceous and Quaternary sediments are distributed in the topographically low parts of this area (Fig. 2).

The Paleozoic volcano-sedimentary sequences in the Almalyk district have been extensively intruded by granitoids, which are estimated to occupy >60% of this region (Fig. 2). The oldest magmatic phase in the vicinity of the Almalyk district is represented

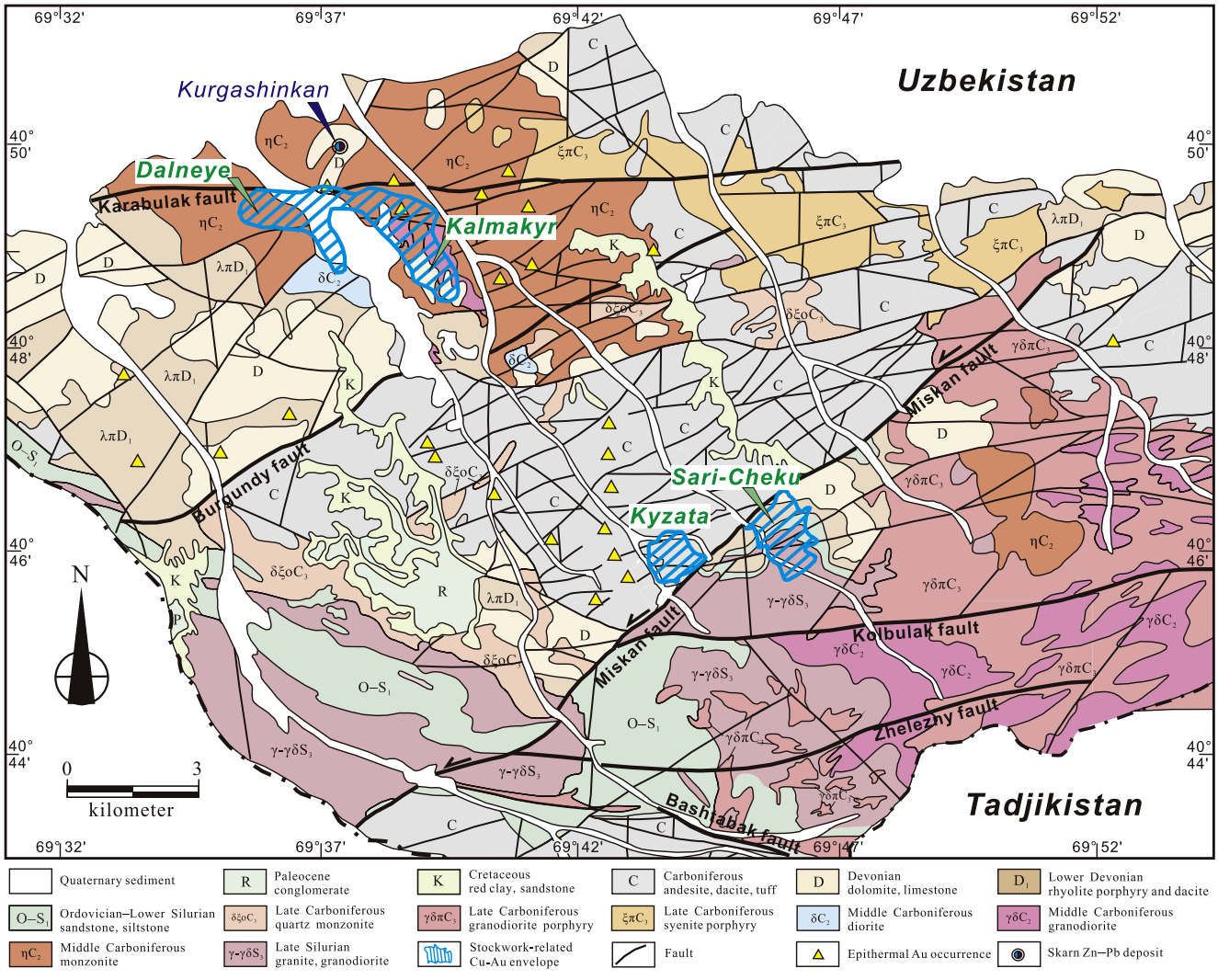

Fig. 2. Geologic map of the Almalyk Cu–Au–polymetallic district, displaying Kalmakyr and other important porphyry Cu–Au, skarn Zn–Pb and epithermal Au deposits, modified from a map presented by the Almalyk Mining–Metallurgical Complex.

by sporadic exposures of a Late Silurian complex of biotite granite, granodiorite, plagiogranite, and alaskite stocks and dikes that extends predominantly south of this area (Fig. 2).

Late Paleozoic intrusive rocks are widely scattered throughout the Almalyk district and principally comprise a gabbrodiorite–diorite–monzonite–granodiorite porphyry–quartz porphyry (Fig. 2). They were subdivided into three main generations of magmatism including the early Devonian quartz porphyry, the middle Carboniferous monzonite–diorite, and the late Carboniferous to early Permian granodiorite porphyry. The early Devonian quartz porphyry generally occurs as interlayers within or upon intermediate to felsic volcano-sedimentary formations. The middle Carboniferous monzonite is the most widespread intrusive phase with occasional transition to diorite and gabbrodiorite (Turamuratov et al., 2011). The late Carboniferous to early Permian granodiorite porphyry (quartz monzonite porphyry in Golovanov et al. (2005) and Seltmann et al. (2014a)) is part of a large intrusion with limited exposure in the middle of the Almalyk district (Fig. 2). These late Paleozoic granitoids are interpreted to be associated with the northward subduction of the Turkestan Ocean beneath the Middle Tien Shan, coeval with the formation of the Beltau–Kurama magmatic arc (Golovanov et al., 2005; Xue et al., 2014). Hydrothermal alteration and related gold–copper mineralization in the Almalyk district are mostly related to the late Carboniferous to early Permian granodiorite porphyry (Golovanov et al., 2005; Seltmann and Porter, 2005) or the middle Carboniferous monzonite (Turamuratov et al., 2011).

The faults in the Almalyk district are complex and mostly steep-dipping faults that display dominant east–west to northeast orientation at the current surface. However, the whole district seems to be controlled by a deep-seated, northwest-trending fault system interpreted from satellite images and geophysical (Golovanov et al., 2005). East–west-trending faults are interpreted to control the localization of mineralization and were reactivated during the Alpine Orogeny (Golovanov et al., 2005). Intersections between northwest and east–west trending faults appear to host major copper–gold mineralization at the Almalyk district (Turamuratov et al., 2011). Northeast-oriented faults postdate the magmatic-hydrothermal mineralization events, probably developed during the Alpine Orogeny (Golovanov et al., 2005).

4. Geology of the Kalmakyr Mine and sampling

4.1. Geological units and relationships

The Kalmakyr porphyry deposit is spatially related to a bell-shaped, NW-trending late Paleozoic intrusive complex (Fig. 3a), which consist of barren late Devonian quartz porphyry, ore-related middle Carboniferous monzonite and diorite and late Carboniferous granodiorite porphyry (Fig. 3). The intrusive complex is believed to be controlled by NW-trending faults based on geophysical data (Golovanov et al., 2005). However these inferred, deep-seated faults are not well manifested at the surface and are not reflected on the geological map (Fig. 3a). The intrusive complex is cut by the high-angle, EW-trending Kalmakyr fault and several NE-trending faults (Fig. 3a). The mineralization is mainly developed within the intrusive complex, straddling the Kalmakyr fault, and generally follows the trend of the intrusion, i.e., trending NW (Fig. 3a). The mineralizing hydrothermal system is interpreted to be focused in zones of cataclasis controlled by the inferred NW-trending faults and the EW-trending Kalmakyr fault. Middle Devonian carbonate (dolomite and limestone) remnants exposed in the deposit area (Fig. 3a) were contact metamorphosed, forming garnet-bearing skarns.

Quartz porphyry crops out in the southern end of the Kalmakyr deposit area (Fig. 3) and is considered to be the sub-volcanic equivalent of the early Devonian intermediate to felsic volcano-sedimentary sequence. The quartz porphyry does not host any mineralization (Fig. 3) and probably represents a pre-mineralization intrusive phase. It contains about 20–30% phenocrysts, which consist of anhedral quartz (15–20%), subhedral sanidine (3–5%) and plagioclase (2–5%) within a fine-grained felsic groundmass. The phenocrysts are very large, ranging from 1 to 2 cm (Fig. 4a and b).

Monzonite is exposed in the northern and central sectors of the Kalmakyr deposit. It is the most widespread ore-hosting intrusive phase (Fig. 3a). This unit, previously named syenodiorite (Meshchaninov and Azin, 1973), consists mainly of coarse, subhedral to euhedral, phenocryst-like plagioclase (40–45%) and K-feldspar (25–30%), with minor amounts of hornblende (4–6%), biotite (3–5%) and anhedral quartz (3–5%) (Fig. 4c and d). Mineralized monzonite contains pyrite–chalcopyrite disseminations and stockworks (Fig. 4c), associated with pervasive sericitization and silicification characterized by sericite replacing plagioclase and fine-grained quartz replacing other minerals (Fig. 4d). In the western sector of the Kalmakyr deposit, the monzonite gradually transits to diorite (Turamuratov et al., 2011; Fig. 3), which mainly comprises equigranular plagioclase (55–60%), hornblende (25–30%) and biotite (5–8%).

Granodiorite porphyry intrudes the earlier monzonite and diorite (Fig. 3b). It contains plagioclase (20–25%), quartz (10–15%), K-feldspar (8–10%), hornblende (6–8%), and sparse biotite (2–4%) phenocrysts set in a fine-grained plagioclase–quartz groundmass, with a phenocryst to groundmass ratio of 1:1 (Fig. 4f). The granodiorite porphyry has undergone widespread potassic alteration, associated with quartz–pyrite–chalcopyrite veinlets and pyrite and chalcopyrite disseminations (Fig. 4e).

4.2. Hydrothermal alteration and mineralization

Mineralization in the Kalmakyr deposit associates with widespread hydrothermal alteration, mainly in monzonite and granodiorite porphyry (Figs. 3 and 5). The types of alteration and their timing and zonation have been well documented by Golovanov et al. (2005).

The early K-silicate alteration, consisting of hydrothermal K-feldspar and silicification in the upper central part of the granodiorite porphyry, forms a barren inner core. This central K-silicate alteration zone grades outwards into a laterally extensive ore-hosting phyllic alteration zone, which is subdivided into two sub-zones, i.e., the quartz–sericite and the quartz–sericite–chlorite–biotite (Turamuratov et al., 2011). The majority of high-grade ores, characterized by chalcopyrite–pyrite–magnetite–molybdenite stockworks and veinlets, as well as development of hematite, is hosted by the quartz–sericite–chlorite–biotite zone. The copper grades are 4–6 times higher in the phyllic zone with strong chlorite alteration than those in the chlorite-barren zone (Golovanov et al., 2005). The phyllic zones are enveloped by a propylitic alteration zone (Fig. 5), with epidote–chlorite–illite assemblage. The propylitic zone hosts pyrite–chalcopyrite–sphalerite–galena veinlets and disseminations with medium copper content.

The majority of copper mineralization at Kalmakyr is hosted by the monzonite, and only minor amounts of low-grade copper ores occur in the granodiorite porphyry surrounding the monzonite (Fig. 3). The granodiorite porphyry at the core of the intrusive complex is barren (Fig. 3a), and is surrounded by high-grade ores (>0.8% Cu), followed by a broader medium-grade zone (average 0.7% Cu) and then a low-grade halo containing 0.1–0.3% copper (Fig. 3a). At Kalmakyr, the dominant mineralization styles are

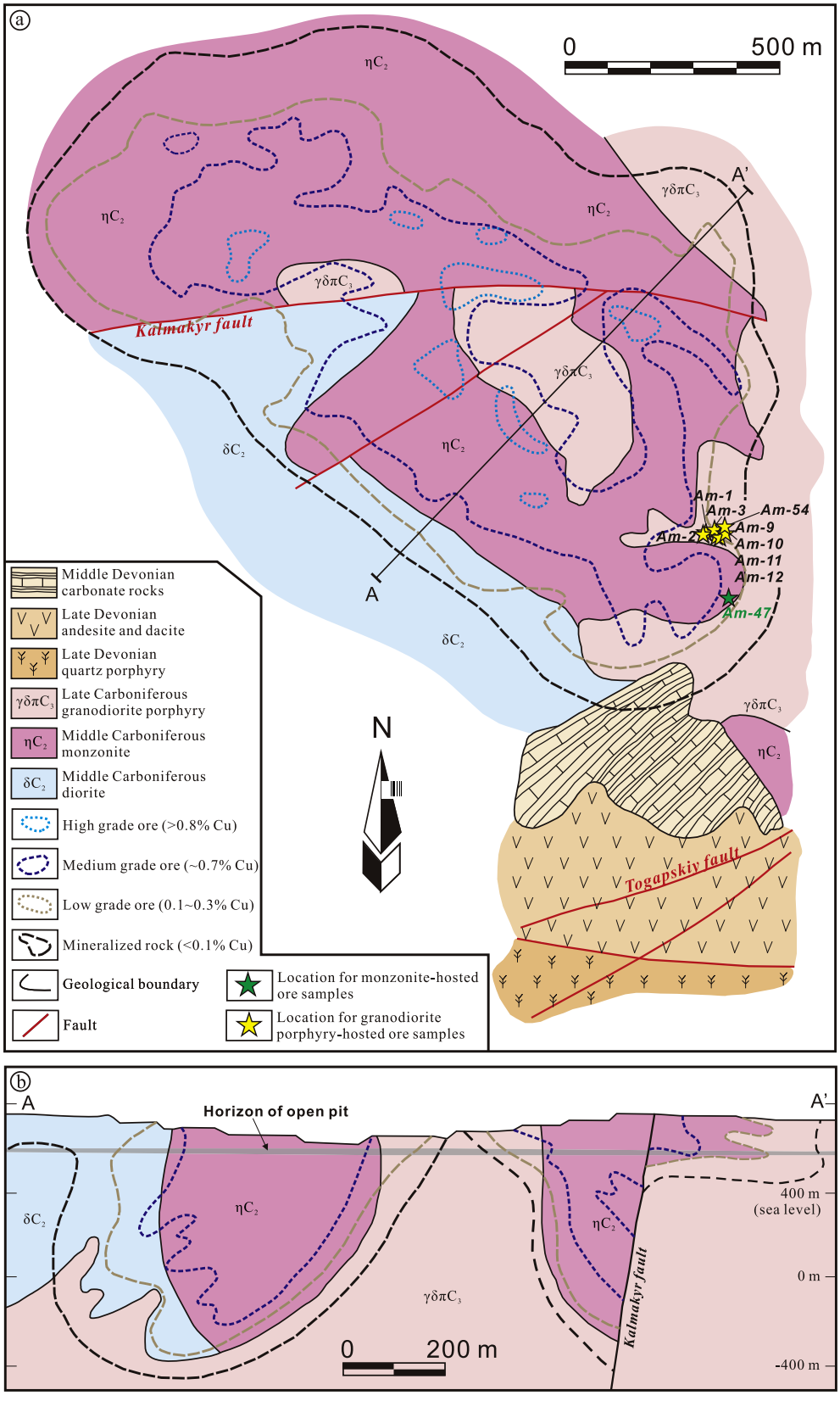

Fig. 3. Simplified geological and grade distribution map (a) and cross-section (b) of the Kalmakyr porphyry gold–copper deposit, after Samonov and Pozharisky (1977), Sokolov (1995) and Golovanov et al. (2005).

stockworks and veinlets of chalcopyrite, pyrite and molybdenite, and disseminated ores are relatively minor (Fig. 5).

According to Golovanov et al. (2005), the mineral assemblages of veinlet and stockwork ores can be divided into the following stages: 1) barren quartz–K-feldspar stockworks (Fig. 5a) and quartz–molybdenite–hematite veinlets (Fig. 5e); 2) quartz–magnetite veinlets (Fig. 5a and b); 3) auriferous quartz–pyrite–chalcopyrite–molybdenite veinlets (Fig. 5b–d, and f), which account for

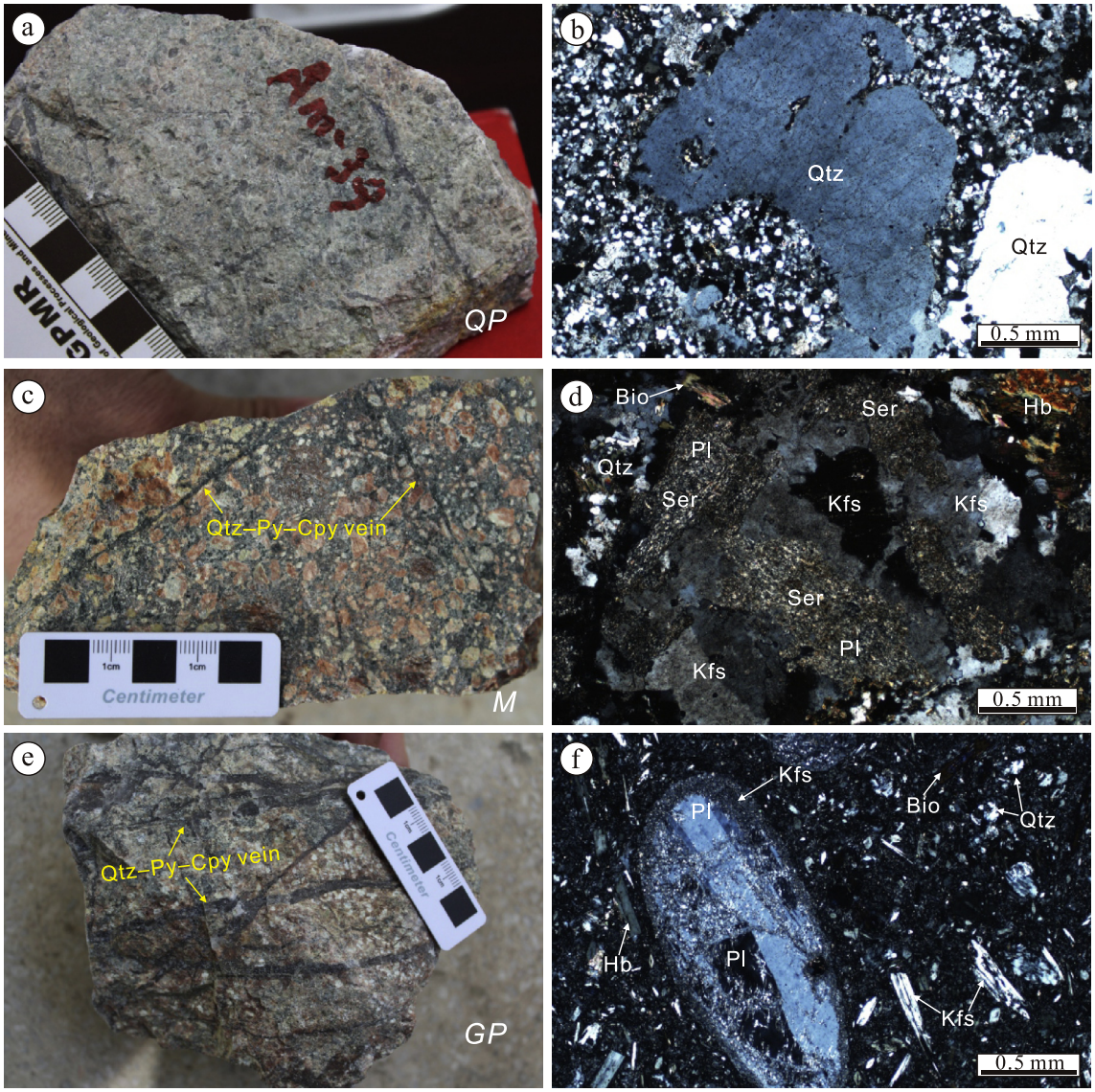

Fig. 4. Photographs and photomicrographs showing the main textures and mineral assemblages of major intrusive phases of the Kalmakyr porphyry deposit. a) weakly silicified barren quartz porphyry; b) porphyritic texture of the quartz porphyry with anhedral quartz phenocrysts under cross-polarized light; c) monzonite with disseminated pyrite and chalcopyrite and stockworks quartz–chalcopyrite–pyrite veinlets (Sample Am-47); d) subhedral to euhedral K-feldspar and sericite-altered plagioclase phenocrysts in monzonite under cross-polarized light (Sample Am-47); e) granodiorite porphyry with disseminated pyrite and chalcopyrite, and quartz–pyrite–chalcopyrite veinlets (Sample Am-54); f) porphyritic granodiorite porphyry showing plagioclase phenocryst partially rimmed by K-feldspar under cross-polarized light (Sample Am-54). Mineral abbreviations: *Qtz* quartz; *Kfs* K-feldspar; *Hb* hornblende; *Bio* biotite; *Ser* sericite; *Py* pyrite; *Cpy* chalcopyrite.

90% of the gold contained in the deposit; 4) quartz–carbonate–polysulfide veinlets accounting for the remaining 10% of gold; 5) zeolite–anhydrite veinlets, and 6) carbonate–barite veinlets.

4.3. Previous age estimates

At Kalmakyr, published K–Ar ages range from 320–280 Ma for unspecified altered rocks to 301–273 Ma for hydrothermal minerals of phlogopite, sericite and hydro-mica (Golovanov et al., 2005). U–Pb zircon dating of fresh and altered monzonite body yielded emplacement ages of 308 ± 1 Ma and 308 ± 4 Ma, respectively, whereas the age of granite porphyry stock (corresponding to granodiorite porphyry in this study) was dated at 315 ± 1 Ma (Seltmann et al., 2011). This age corresponds well with the U–Pb age of an altered quartz syenite dated at 315 ± 2 Ma (Dolgopolova et al., 2016). However, the published ages of these two intrusive phases are inconsistent with geological evidence showing that the granodiorite porphyry intrudes the monzonite (Fig. 3b). Re–Os molybdenite age of 314 Ma from Kalmakyr deposit has been reported by Seltmann et al. (2014b), but without any description of dating samples and analytical errors.

Several isotopic ages have also been published for the Sari-Cheku porphyry Cu–Au deposit ~10 km southeast of Kalmakyr (Fig. 2). Zircon U–Pb age dating from the ore-bearing granodiorite porphyry and post-ore granite yielded ages of 306 ± 3 Ma and 297 ± 3 Ma (Seltmann et al., 2011), respectively. Microgranite-porphyry and andesite-dacite from the Sari-Cheku open pit yielded U–Pb ages of 304 ± 3 Ma and 311 ± 3 Ma (Dolgopolova et al., 2016), respectively, but their relationship with Cu–Au porphyry mineralization are not clear. Xue et al. (2013) reported molybdenite model ages between 329.6 ± 4.9 Ma and 315.4 ± 4.5 Ma from stockwork ores of the Sari-Cheku deposit, suggesting a long-lived magmatic-hydrothermal system, while a weighted average age of

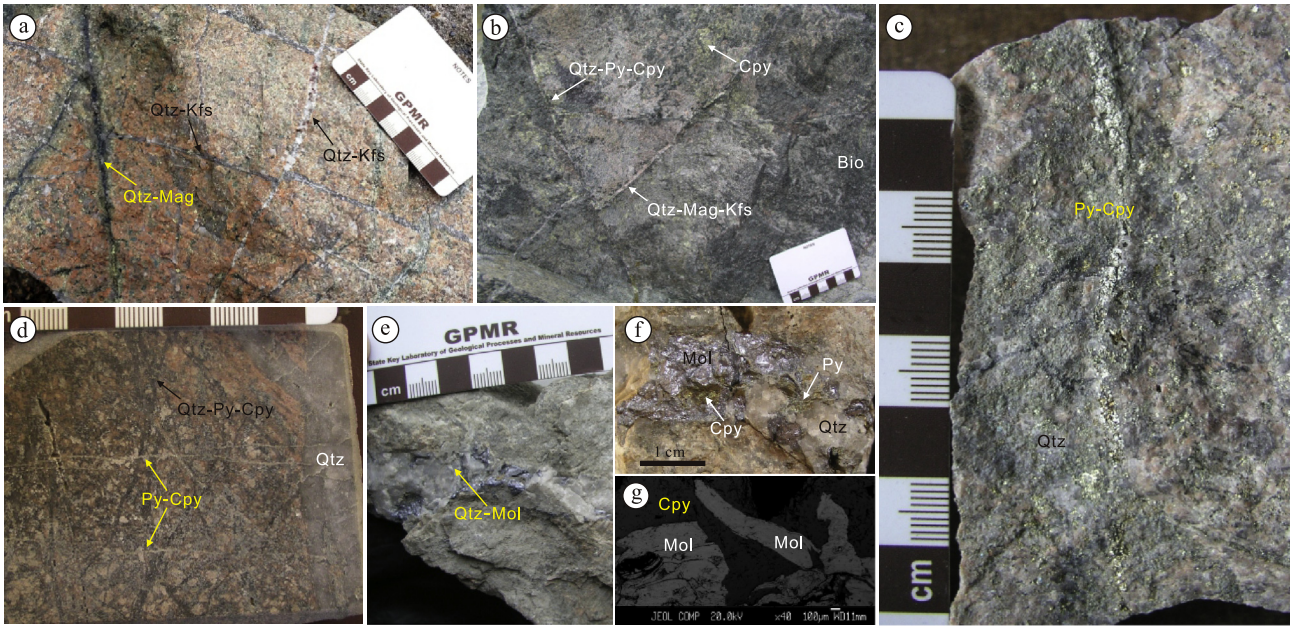

Fig. 5. Representative stockwork copper ores from the Kalmakyr. a) early stockwork quartz–K-feldspar (stage 1) cut by quartz–magnetite veinlets (stage 2) with intense chlorite alteration; b) quartz–magnetite veinlets with disseminated K-feldspar (stage 2) cut by quart–pyrite–chalcopyrite veinlets (stage 3) with intense biotite alteration; c–d) dense quartz–pyrite–chalcopyrite stockworks and disseminations (stage 3) with severe silicification and potassic alterations; e) quartz–molybdenite veinlets of stage 1 (sample Am-3); f) quartz–pyrite–chalcopyrite–molybdenite veinlets of stage 3 (sample Am-1); g) a scanning electron microprobe image showing the intergrowth relationships between chalcopyrite and molybdenite (Sample Am-2). Mineral abbreviations: *Qtz* quartz; *Kfs* K-feldspar; *Bio* biotite; *Ser* sericite; *Py* pyrite; *Cpy* chalcopyrite; *Mol* molybdenite; *Mag* magnetite.

317.6 ± 2.5 Ma is thought to represent the time for copper mineralization.

4.4. Sampling

In order to determine more accurately the ages of porphyry Cu–Au–Mo mineralization and related magmatism at Kalmakyr, we collected samples of the two principal ore-related magmatic rocks (monzonite and granodiorite porphyry) for zircon U–Pb dating, rare earth elements and Lu–Hf isotopes in zircons, and seven molybdenite-bearing samples for Re–Os dating. All studied samples were collected from the 520 m mRL (48°48′21″N, 69°39′07″E and 48°48′26″N, 69°39′07″E) in the Kalmakyr open pit (Fig. 3a). Sample Am-47 is a monzonite with disseminated pyrite and chalcopyrite and quartz–chalcopyrite–pyrite stockworks (Fig. 4c and d). Sample Am-54 is a granodiorite porphyry with quartz–pyrite–chalcopyrite stockworks (Fig. 4e and f). Two of seven molybdenite-bearing samples (Am-3 and Am-11) are from the stage-1 quartz–molybdenite veinlets in chlorite-altered and silicified granodiorite porphyry (Fig. 5e), and the other five samples (Am-1, Am-2, Am-9, Am-10 and Am-12) are from the stage-3 quartz–pyrite–chalcopyrite–molybdenite stockworks in potassic altered and silicified granodiorite porphyry (Fig. 4f). For detailed description of each sample are shown in Table 1.

5. Analytical techniques

5.1. Zircon U–Pb dating and rare earth element

Zircon grains were extracted using conventional heavy liquids and magnetic separation techniques, then handpicked under a binocular microscope. Selective zircon grains were mounted in an epoxy resin and polished to expose the grain center. The mounts were photographed under transmitted and reflected light and cathodoluminescence (CL) to examine the internal structure of zircon crystals and choose potential target for U–Pb and Lu–Hf isotope analyses.

Laser ablation inductively coupled plasma mass spectrometry (LA-ICP-MS) zircon U–Pb and rare earth element analyses were performed simultaneously on an Agilent 7500a ICP-MS, equipped with a 193-nm ArF-excimer laser (GeoLas 2005) at the State Key Laboratory of Continental Dynamics in Northwest University, Xi'an, China. The spot diameter for each analysis was 32 μm.

Table 1
Description of the studied samples from the Kalmakyr deposit.

Sample	Description of sample	Main ore minerals	Location
Am-3	Cu–Mo mineralization in veinlets in chlorite-altered and silicified	Molybdenite, chalcopyrite	Kalmakyr open pit @ 520 mRL
Am-11	granodiorite porphyry (stage-1 quartz–molybdenite veinlets)	Molybdenite	48°48′21″N, 69°39′07″E
Am-1	Cu–Mo mineralization in stockworks in potassic-altered and silicified	Pyrite, chalcopyrite, molybdenite, gold	
Am-2	granodiorite porphyry (stage-3 quartz–pyrite–chalcopyrite–molybdenite stockworks)	Chalcopyrite, molybdenite	
Am-9		Molybdenite, chalcopyrite, pyrite	
Am-10		Pyrite, molybdenite, gold	
Am-12		Molybdenite, chalcopyrite, gold	
Am-54	Granodiorite porphyry with disseminated Cu–Mo mineralization	Pyrite, chalcopyrite, molybdenite, gold	
Am-47	Monzonite with disseminated and stockwork Cu mineralization	Pyrite, chalcopyrite, gold	Kalmakyr open pit @ 520 mRL 48°48′26″N, 69°39′07″E

Helium was used as the carrier gas to enhance transport efficiency of the ablated material. The helium carrier gas inside the ablation cell was mixed with argon before entering the inductively coupled plasma to maintain stable and optimum excitation conditions. Detailed operating condition and procedures were described by Yuan et al. (2004). Concentrations of U, Th, Pb and other trace elements were calculated using ^{29}Si as an internal standard and NIST SRM 610 as the external standard. Zircon 91500 was used as the external standard for both instrumental mass deviation and depth-dependent elemental and isotopic fractionation. The $^{207}Pb/^{206}Pb$ and $^{206}Pb/^{238}U$ ratios were calculated using the GLITTER program, and common Pb was evaluated following the method proposed by Andersen (2002). Zircon Ce anomalies (Ce^{4+}/Ce^{3+}) were calculated using the method based on lattice strain model proposed by Ballard et al. (2002), and age calculations and plotting of concordia diagrams were carried out using ISOPLOT (version 3.0) program (Ludwig, 2003).

5.2. Zircon Lu–Hf isotope analyses

In-situ zircon Lu–Hf isotopic analyses were conducted on the U–Pb dated spot, using a Nu Plasma Multi-Collector (MC)-ICP-MS (Nu Instruments Ltd., UK) attached to a 193-nm ArF-excimer laser at the State Key Laboratory of Continental Dynamics in Northwest University, Xi'an, China. During the analyses, a laser pulse frequency of 8 Hz and a spot size of 44 μm were used. Detailed instrumental conditions and data acquisition were described by Yuan et al. (2008). Interference of ^{176}Yb on ^{176}Hf was corrected by measuring the intensity of the interference-free ^{175}Lu, and the recommended $^{176}Lu/^{177}Hf$ ratio of 0.02669 (De Bievre and Taylor, 1993) was used to calculate $^{176}Lu/^{177}Hf$ ratios. Correction of the isobaric interference of ^{176}Yb on ^{176}Hf and calculation of $^{176}Hf/^{177}Hf$ ratios were performed by using the recommended $^{176}Yb/^{172}Yb$ ratio of 0.5886 (Chu et al., 2002). During analyses, the $^{176}Hf/^{177}Hf$ ratios for standard 91500 and GJ-1 are 0.282315 ± 12 (2σ, N = 24) and 0.282023 ± 14 (2σ, N = 24), respectively, which are in good agreement with the recommended values of 0.282015 ± 19 (2σ) for GJ-1 (Elhlou et al., 2006) and 0.282303 ± 8 (2σ) for 91500 (Goolaerts et al., 2004), respectively. Analytical errors for $^{176}Yb/^{177}Hf$, $^{176}Lu/^{177}Hf$ and $^{176}Hf/^{177}Hf$ are reported in 2σ. The decay constant of 1.865×10^{-11} $year^{-1}$ (Scherer et al., 2001), initial chondritic reservoir (CHUR) ratios of $^{176}Hf/^{177}Hf = 0.282772$ and $^{176}Lu/^{177}Hf = 0.0332$ from Belousova et al. (2002) were adopted in isotopic calculations. The depleted mantle Hf model ages (T_{DM}) were calculated relative to the depleted mantle with the present-day $^{176}Hf/^{177}Hf$ ratio of 0.28325 and $^{176}Lu/^{177}Hf$ ratio of 0.0384 (Griffin et al., 2002). The crustal Hf model ages (T_{DM}^{C}) were calculated by referring to a $^{176}Lu/^{177}Hf$ ratio of 0.015 for the average continental crust (Griffin et al., 2002).

5.3. Molybdenite Re–Os analytical methods

Molybdenite samples were separated by liquid and magnetic techniques, followed by flotation using high-purity water before handpicked under a binocular microscope. The purity of the samples was better than 99%. Re–Os isotopic analyses were undertaken by a Thermo ICP-MS (TJA X-series) at the National Research Center of Geoanalysis, Chinese Academy of Geosciences, following the method described in Du et al. (2004). Molybdenite ages were calculated using a ^{187}Re decay constant of 1.666×10^{-11} $year^{-1}$ (Smoliar et al., 1996). Uncertainty in Re–Os model ages contains 1.02% uncertainty in the ^{187}Re decay constant and uncertainty in Re and Os concentrations, which includes weighing errors for both spike and sample, and uncertainty in spike calibration and mass spectrometry analytical error; the confidence level is 95%. Blanks during the course of the analysis were <2.9 pg/g for Re and <0.4 pg/g for Os^{187}. The national standard molybdenite (GBW04435) yielded 17.21 ± 0.27 pg/g for Re and 25.27 ± 0.21 pg/g for Os^{187}, which are similar with uncertainty to the recommended values (17.39 ± 0.32 pg/g for Re and 25.46 ± 0.60 pg/g for Os^{187} (Du et al., 2004). Furthermore, Re–Os model ages of the molybdenite reference (GBW04435) recorded in this study (140.1 ± 2.8 Ma), are in good agreement with their accepted value of 139.6 ± 3.8 Ma (Du et al., 2004).

6. Results

6.1. Zircon LA-ICP-MS U–Pb data

The zircon U–Pb isotope results of mineralized monzonite (sample Am-47) and granodiorite porphyry (sample Am-54) are presented in Table 2. The majority of analytical results yielded concordant ages, and the few exceptions (i.e., spots 5, 9 and 20 of sample Am-47 and spot 16 of sample Am-54, Table 2) were excluded from weighted average age calculation.

Zircon grains from the monzonite (sample Am-47) are between 200 and 400 μm in length, with an aspect ratio of 1:1 to 3.5:1. They are colorless to light pink, exhibit clear oscillatory zoning, but most of them are not complete crystals or are not euhedral (Fig. 6a). The measured zircon Th/U ratios range from 0.3 to 0.9 (Table 2), much higher than those of metamorphic origin (<0.2; Rubatto, 2002), thus indicating a magmatic origin (Hoskin and Ireland, 2000). Twenty-four out of 27 analyses (Table 2) produced concordant ages, which yielded a weighted average $^{206}Pb/^{208}U$ age of 327.2 ± 5.6 Ma (MSWD = 3.5) (Fig. 7a).

Zircon grains from the granodiorite porphyry (sample Am-54) are colorless and transparent, with lengths ranging from 150 to 300 μm and length/width ratios between 2:1 and 3:1. They are euhedral, have elongated shape with typical oscillatory zoning (Fig. 6b), and have Th/U ratios ranging from 0.3 to 0.7 (Table 2), which is consistent with a magmatic origin. Twenty-nine out of 30 analyses produced concordant ages, which yielded a weighted average $^{206}Pb/^{208}U$ age of 313.6 ± 2.8 (MSWD = 0.2) (Fig. 7b).

6.2. Rare earth element pattern in zircon

Rare earth element (REE) concentrations in zircon from monzonite (Am-47) and granodiorite porphyry (Am-54) are shown in Table 3. Chondrite-normalized REE patterns of zircon are presented in Fig. 8. Zircon grains from both monzonite and granodiorite porphyry yielded similar REE patterns that are characterized by a deficit of light REE and enrichment of heavy REE, together with positive Ce and variably negative Eu anomalies (Fig. 8), suggesting a typical magmatic origin (Belousova et al., 2002; Hoskin and Ireland, 2000). Zircon grains of sample Am-47 have total REE varying from 1097 to 362 ppm, Eu_N/Eu_N^* from 0.57 to 0.20, and Ce^{4+}/Ce^{3+} from 1074 to 387, whereas zircon grains of sample Am-54 have total REE varying from 859 to 344 ppm, Eu_N/Eu_N^* from 1.02 to 0.41, and Ce^{4+}/Ce^{3+} from 1621 to 642 (Table 3).

6.3. Zircon Lu–Hf isotopes

The Lu–Hf isotope results for zircon grains from monzonite (Am-47) and granodiorite porphyry (Am-54) are presented in Table 4. Fifteen spots were analyzed for each sample. Zircon grains from the monzonite sample have variable $\varepsilon_{Hf}(t)$ values from +11 to +1.7, with corresponding crustal model ages (T_{DM}^{C}) from 1243 to 641 Ma (Table 4; Fig. 9). In contrast, zircons from the granodiorite porphyry sample have relative homogeneous $\varepsilon_{Hf}(t)$ values from

Table 2
LA-ICP-MS analytical results of zircon U–Pb isotopic ratios and ages of magmatic rocks from the Kalmakyr deposit.

Spot	Th/U	Measured isotope ratio						Apparent ages (Ma)						Note
		$^{207}Pb/^{206}Pb$	1σ	$^{207}Pb/^{235}U$	1σ	$^{206}Pb/^{238}U$	1σ	$^{207}Pb/^{206}Pb$	1σ	$^{207}Pb/^{235}U$	1σ	$^{206}Pb/^{238}U$	1σ	
Sample Am-47 (ore-hosting monzonite)														
1	0.5	0.05259	0.00238	0.39616	0.01600	0.05466	0.00130	311	100	339	12	343	8	
2	0.6	0.04972	0.00191	0.32834	0.01076	0.04791	0.00110	182	87	288	8	302	7	
3	0.5	0.05004	0.00201	0.37200	0.01293	0.05393	0.00125	197	91	321	10	339	8	
4	0.9	0.04897	0.00209	0.36502	0.01366	0.05408	0.00127	146	97	316	10	340	8	
5	0.7	0.06184	0.00243	0.45703	0.01533	0.05361	0.00125	669	82	382	11	337	8	Disconcordant
6	0.8	0.05242	0.00188	0.39075	0.01166	0.05407	0.00123	304	80	335	9	340	8	
7	0.4	0.05130	0.00201	0.37583	0.01257	0.05313	0.00122	254	88	324	9	334	7	
8	0.6	0.05333	0.00203	0.39242	0.01266	0.05336	0.00122	343	84	336	9	335	7	
9	0.6	0.05006	0.00259	0.31384	0.01479	0.04547	0.00110	198	116	277	11	287	7	Disconcordant
10	0.5	0.04951	0.00186	0.36051	0.01144	0.05280	0.00120	172	86	313	9	332	7	
11	0.7	0.04995	0.00179	0.36481	0.01077	0.05296	0.00119	193	81	316	8	333	7	
12	0.6	0.04864	0.00185	0.34101	0.01091	0.05083	0.00114	131	87	298	8	320	7	
13	0.7	0.05153	0.00206	0.38788	0.01326	0.05457	0.00124	265	89	333	10	343	8	
14	0.3	0.05164	0.00172	0.39136	0.01029	0.05495	0.00121	270	74	335	8	345	7	
15	0.7	0.04978	0.00212	0.34871	0.01289	0.05079	0.00116	185	96	304	10	319	7	
16	0.4	0.05030	0.00206	0.33418	0.01179	0.04817	0.00109	209	92	293	9	303	7	
17	0.5	0.05225	0.00193	0.36967	0.01128	0.05129	0.00114	296	82	319	8	322	7	
18	0.4	0.04958	0.00216	0.37813	0.01435	0.05529	0.00126	175	98	326	11	347	8	
19	0.5	0.05299	0.00235	0.38750	0.01506	0.05302	0.00122	328	98	333	11	333	7	
20	0.7	0.05659	0.00289	0.32146	0.01476	0.04118	0.00098	475	110	283	11	260	6	Disconcordant
21	0.6	0.05002	0.00182	0.36064	0.01076	0.05226	0.00115	196	83	313	8	328	7	
22	0.6	0.05184	0.00218	0.36411	0.01320	0.05091	0.00115	278	94	315	10	320	7	
23	0.6	0.04990	0.00205	0.33231	0.01167	0.04827	0.00108	191	93	291	9	304	7	
24	0.5	0.05555	0.00209	0.40504	0.01254	0.05285	0.00116	434	81	345	9	332	7	
25	0.8	0.05419	0.00206	0.36952	0.01162	0.04943	0.00109	379	83	319	9	311	7	
26	0.4	0.05117	0.00204	0.36725	0.01234	0.05203	0.00115	248	89	318	9	327	7	
27	0.5	0.05065	0.00214	0.36975	0.01344	0.05292	0.00118	225	95	320	10	332	7	
Sample Am-54 (ore-bearing granodiorite porphyry)														
1	0.3	0.05426	0.00272	0.37397	0.01701	0.04999	0.00124	382	108	323	13	314	8	
2	0.4	0.04806	0.00236	0.33481	0.01486	0.05053	0.00123	102	112	293	11	318	8	
3	0.4	0.05140	0.00247	0.35292	0.01529	0.04980	0.00121	259	107	307	11	313	7	
4	0.3	0.05280	0.00253	0.36841	0.01592	0.05061	0.00124	320	105	319	12	318	8	
5	0.4	0.05324	0.00251	0.36955	0.01560	0.05034	0.00122	339	103	319	12	317	8	
6	0.4	0.04899	0.00261	0.33169	0.01620	0.04911	0.00122	147	120	291	12	309	7	
7	0.7	0.05417	0.00217	0.36982	0.01277	0.04951	0.00117	378	87	320	9	312	7	
8	0.3	0.05015	0.00221	0.34861	0.01357	0.05041	0.00120	202	99	304	10	317	7	
9	0.4	0.05199	0.00214	0.35871	0.01288	0.05004	0.00118	285	92	311	10	315	7	
10	0.4	0.05127	0.00213	0.35759	0.01298	0.05058	0.00119	253	93	310	10	318	7	
11	0.3	0.05301	0.00244	0.36893	0.01515	0.05048	0.00121	329	101	319	11	317	7	
12	0.3	0.05095	0.00268	0.34984	0.01684	0.04980	0.00123	239	117	305	13	313	8	
13	0.4	0.04903	0.00270	0.33642	0.01701	0.04976	0.00124	150	124	295	13	313	8	
14	0.4	0.05087	0.00298	0.35356	0.01919	0.05040	0.00128	235	130	307	14	317	8	
15	0.4	0.05222	0.00222	0.36217	0.01353	0.05030	0.00119	295	94	314	10	316	7	
16	0.4	0.05849	0.00354	0.39410	0.02211	0.04887	0.00127	548	127	337	16	308	8	Disconcordant
17	0.5	0.04980	0.00209	0.33835	0.01241	0.04927	0.00116	186	95	296	9	310	7	
18	0.3	0.05473	0.00335	0.38025	0.02162	0.05039	0.00131	401	131	327	16	317	8	
19	0.3	0.05078	0.00213	0.34715	0.01274	0.04958	0.00116	231	94	303	10	312	7	
20	0.3	0.05169	0.00220	0.35411	0.01320	0.04967	0.00117	272	95	308	10	313	7	
21	0.4	0.05155	0.00298	0.35633	0.01904	0.05013	0.00126	265	127	310	14	315	8	
22	0.4	0.05127	0.00204	0.35304	0.01207	0.04993	0.00116	253	89	307	9	314	7	
23	0.4	0.05181	0.00247	0.35748	0.01527	0.05003	0.00120	277	105	310	11	315	7	
24	0.4	0.05079	0.00213	0.34887	0.01275	0.04980	0.00116	231	94	304	10	313	7	
25	0.4	0.05466	0.00250	0.37348	0.01522	0.04954	0.00118	399	99	322	11	312	7	
26	0.4	0.05164	0.00250	0.35146	0.01535	0.04935	0.00118	269	107	306	12	311	7	
27	0.4	0.05324	0.00345	0.35711	0.02161	0.04863	0.00127	339	140	310	16	306	8	
28	0.3	0.05283	0.00239	0.35200	0.01414	0.04830	0.00114	322	99	306	11	304	7	
29	0.4	0.04729	0.00244	0.32380	0.01524	0.04964	0.00120	63	119	285	12	312	7	
30	0.4	0.04960	0.00276	0.34316	0.01755	0.05016	0.00124	176	125	300	13	316	8	

+5.7 to −1.8 and older crustal model ages (T^{C}_{DM}) varying from 1443 Ma to 959 Ma (Table 4; Fig. 9).

6.4. Re–Os molybdenite ages

The analytical results of Re–Os isotopes of seven molybdenite samples are presented in Table 5. The ^{187}Re and ^{187}Os concentrations range from 62 to 565 ppm and from 320 to 2955 ppb, respectively (Table 5). Two molybdenite samples from the quartz–molybdenite veins (stage-1) show a narrow range of Re–Os model ages from 313.2 ± 7.2 Ma to 312.2 ± 4.7 Ma (Table 5). Five molybdenite samples from the quartz–pyrite–chalcopyrite–molybdenite vein (stage-3) yielded model ages ranging from 310.4 ± 5.2 Ma to 306.3 ± 4.3 Ma (Table 5), with a well-constrained isochron age of 307.6 ± 2.5 Ma (MSWD = 0.5; N = 5) and a weighted mean age of 308.6 ± 2.1 Ma (MSWD = 0.4; N = 5) (Fig. 10a). All seven molybdenite samples together exhibit a well-constrained isochron age of 309.1 ± 2.2 Ma (MSWD = 1.3;

Fig. 6. Cathodoluminescence images of zircon grains with U–Pb (yellow circles) and Lu–Hf (white circles) dating spots, with $^{206}Pb/^{238}U$ ages and $\varepsilon_{Hf}(t)$ values for monzonite (a) and granodiorite porphyry (b) from the Kalmakyr deposit.

N = 7) and a weighted mean age of 310.4 ± 5.2 Ma (MSWD = 0.8; N = 7), with an initial $^{187}Os/^{188}Os$ ratio of 0.9 ± 4.9 (Fig. 10b).

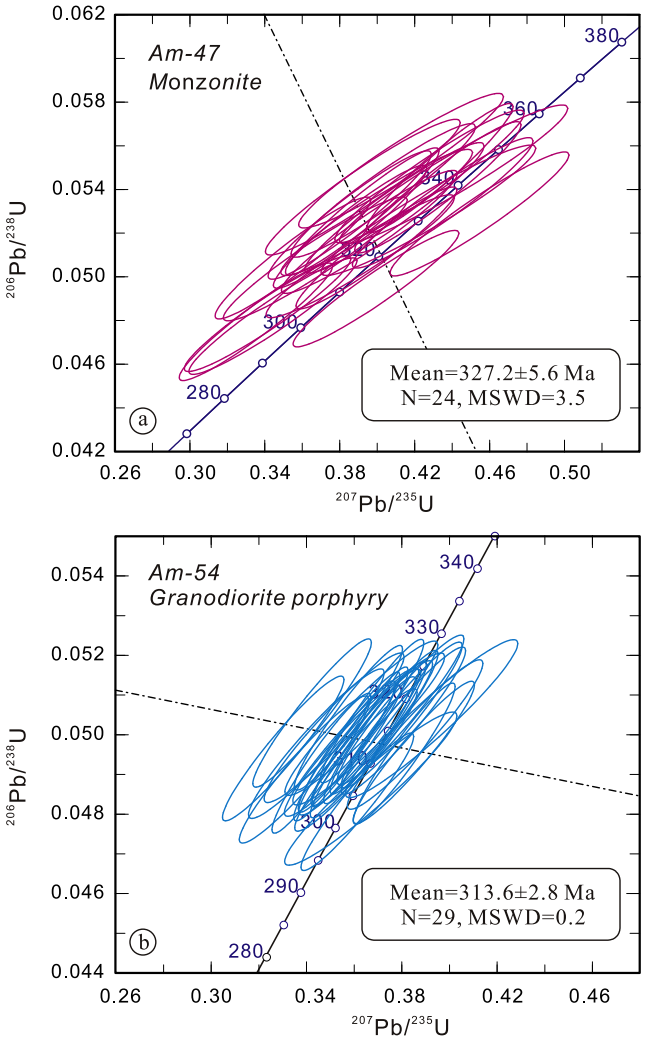

Fig. 7. Concordia diagrams of zircon samples from the monzonite (a) and granodiorite porphyry (b) from the Kalmakyr deposit.

7. Discussion

7.1. Timing of magmatism and related mineralization

In order to determine the relationship between magmatism and porphyry mineralization and understand the mineralization processes, it is important to accurately determine the ages of emplacement of magmatic intrusions and mineralization (Chiaradia et al., 2013). U–Pb dating of magmatic zircon is currently regarded as the most reliable proxy for emplacement ages of magmatic intrusions due to the high closure temperature (>900 °C; Lee et al., 1997), and Re–Os dating of molybdenite, with a high internal precision (<0.2%; Stein et al., 2001), is regarded as the most reliable method to determine the ages of mineralization.

A number of isotopic ages has been obtained for various rocks and minerals from the Kalmakyr deposit and the nearby Sari-Cheku deposit, as summarized in Fig. 11. The wide range of K–Ar ages reported by Golovanov et al. (2005) on sericite and bulk rock samples from the Kalmakyr deposit, ranging from 320 to 273 Ma (Fig. 11), reflects multiple magmatic activities, different closing temperatures, and variable degrees of disturbance of the K–Ar system related to uplift of the Middle Tien Shan. These ages cannot be used to accurately determine the ages of magmatism and mineralization. Previous U–Pb geochronological studies of ore-related intrusions in the Kalmakyr deposit (Seltmann et al., 2011) yielded older ages for granodiorite porphyry (315 ± 1 Ma) than those for monzonite (308 ± 1 Ma and 308 ± 4 Ma), which is contradictory with the observation that the granodiorite porphyry crosscuts the monzonite (Fig. 3b). Dolgopolova et al. (2016) reported zircon U–Pb ages of 315 ± 2 Ma and 422 ± 4 Ma for altered quartz syenite and granosyenite porphyry at Kalmakyr, respectively, but the relationship between these intrusions and copper porphyry mineralization are not clear. As for the Sari-Cheku deposit, the Re–Os molybdenite age (317.6 ± 2.5 Ma; Xue et al., 2013) is older than the U–Pb age of the ore-bearing stock (306 ± 3 Ma; Seltmann et al., 2011), again creating inconsistency.

The U–Pb isotopic data of a large number of magmatic zircon grains from the ore-related intrusions in the Kalmakyr deposit obtained in this study using LA-ICP-MS yielded well defined concordia ages for the monzonite (327.2 ± 5.6 Ma; Fig. 7a) and granodiorite porphyry (313.6 ± 2.8 Ma; Fig. 7b). Thus, the granodiorite porphyry is 13.6 Ma younger than the monzonite, which is consistent with geological observations. Combining previous SHRIMP

Table 3
LA-ICP-MS analytical results of zircon trace elements (in ppm), Eu_N/Eu^*_N, Ce^{4+}/Ce^{3+}, and Ce/Nd ratios of magmatic rocks in the Kalmakyr deposit.

Spot	La	Ce	Pr	Nd	Sm	Eu	Gd	Tb	Dy	Ho	Er	Tm	Yb	Lu	Th	U	Hf	Eu_N/Eu^*_N	Ce^{4+}/Ce^{3+}	Ce/Nd	Apparent age (Ma)
Am-47 (ore-hosting monzonite)																					
1	<0.08	8.46	0.02	0.91	2.14	0.40	10.26	3.47	40.84	15.00	68.69	15.53	162.45	33.71	154.98	337.67	9671	0.26	427	9.3	343
2	0.59	13.82	1.20	8.80	10.68	3.47	32.04	10.02	99.41	32.60	142.85	30.45	303.33	61.69	361.01	626.62	9619	0.57	699	1.6	302
3	0.02	10.46	0.09	1.29	2.81	0.41	13.86	4.39	51.81	19.31	90.97	21.00	225.27	46.88	292.66	612.90	10607	0.20	529	8.1	339
4	0.18	11.77	0.42	4.47	7.28	1.63	28.67	9.30	98.17	33.99	148.32	31.63	314.43	63.01	478.04	544.22	9475	0.35	595	2.6	340
5	0.12	12.16	0.48	5.20	8.92	1.56	34.17	11.02	114.68	40.45	176.40	36.90	358.51	69.65	394.04	593.35	9319	–	–	2.3	Disconcordant
6	0.24	15.77	0.69	7.99	10.03	2.35	41.12	13.89	147.82	51.62	219.65	46.87	450.37	88.69	649.44	855.08	8744	0.35	798	2.0	340
7	0.17	17.09	0.32	2.88	3.37	0.99	16.19	5.48	62.13	24.12	118.30	27.40	294.35	62.95	346.81	874.92	12308	0.41	865	5.9	334
8	0.14	12.41	0.49	5.97	8.31	1.60	33.01	10.39	111.96	40.00	172.57	37.09	363.89	71.64	394.09	628.94	9557	0.30	628	2.1	335
9	0.50	15.87	0.77	7.67	11.49	3.63	44.63	14.32	141.87	46.22	185.41	37.78	361.24	69.01	334.39	540.17	11595	–	–	2.1	Disconcordant
10	<0.00	13.67	0.03	1.10	2.23	0.29	13.09	4.49	50.97	20.37	95.81	22.08	236.03	49.08	344.08	729.24	11105	0.16	692	12.4	332
11	0.07	12.96	0.45	5.16	9.42	1.85	42.05	13.18	138.62	48.09	206.82	43.79	428.73	84.46	562.72	762.70	8999	0.28	656	2.5	333
12	0.01	12.25	0.23	4.29	7.58	1.01	34.15	10.85	115.49	40.51	178.67	37.61	372.39	72.60	393.24	607.74	9868	0.19	620	2.9	320
13	0.07	10.82	0.28	4.27	7.58	1.32	35.52	10.29	110.88	38.13	160.52	34.40	340.03	66.06	358.98	513.20	8281	0.25	547	2.5	343
14	0.01	21.20	0.13	2.38	4.16	0.72	20.54	7.46	93.52	36.82	190.57	45.19	493.75	108.95	507.83	1557.41	9714	0.24	1074	8.9	345
15	<0.05	12.51	0.34	3.86	7.54	1.37	32.49	11.17	127.20	46.08	201.91	42.46	428.92	83.09	582.42	801.10	10059	0.27	633	3.2	319
16	0.21	11.49	0.56	6.03	6.42	1.82	20.42	6.53	66.43	21.73	97.27	20.90	214.34	43.73	205.78	462.05	9549	0.49	581	1.9	303
17	0.06	11.69	0.23	2.39	3.74	0.88	17.48	5.63	64.30	23.64	110.32	25.00	259.80	55.39	312.83	641.28	9055	0.33	591	4.9	322
18	<0.00	7.66	<0.042	1.12	2.53	0.39	9.02	3.36	40.91	15.48	73.52	16.61	179.61	38.06	149.38	374.91	8896	0.25	387	6.8	347
19	0.05	8.48	0.19	2.31	5.01	0.79	18.99	6.07	66.27	23.68	102.03	22.03	220.61	44.05	192.14	355.25	9211	0.25	429	3.7	333
20	0.67	20.87	1.91	16.64	20.05	6.91	60.85	20.24	180.68	54.70	218.18	43.70	409.95	79.29	455.52	631.46	11770	–	–	1.3	Disconcordant
21	0.19	12.17	0.28	3.84	6.41	1.14	29.91	9.62	106.17	38.41	166.58	36.51	361.13	72.83	465.25	729.56	8836	0.25	616	3.2	328
22	0.08	9.82	0.28	3.81	5.32	1.43	24.08	7.72	81.58	28.05	121.07	24.93	250.32	49.31	261.33	418.51	9032	0.39	496	2.6	320
23	0.33	12.42	0.60	5.55	7.27	2.16	23.30	7.18	74.17	23.99	103.11	22.54	231.37	48.29	332.11	590.25	9954	0.51	628	2.2	304
24	0.48	13.03	0.81	6.87	7.89	2.53	25.36	8.11	85.68	28.61	125.40	27.37	287.13	59.65	369.68	700.37	8754	0.55	659	1.9	332
25	0.50	15.33	1.23	10.38	12.65	3.85	41.30	13.16	126.79	41.13	169.04	34.78	338.12	66.04	471.97	597.32	9450	0.52	776	1.5	311
26	0.02	9.43	0.15	1.65	2.62	0.60	13.60	4.34	50.97	20.10	95.89	22.39	236.01	50.75	195.88	508.25	9011	0.31	477	5.7	327
27	0.10	11.10	0.35	4.54	5.74	1.29	22.60	7.15	73.63	26.15	114.91	24.43	246.18	49.20	236.56	447.42	9689	0.35	561	2.4	332
whole-rock	10.80	22.70	3.05	13.90	3.06	0.69	2.60	0.48	2.41	0.47	1.27	0.22	1.49	0.22	13.00	3.58					
Am-54 (ore-bearing granodiorite porphyry)																					
1	0.19	18.20	0.16	1.84	2.01	0.88	6.23	2.33	25.81	10.87	56.28	14.26	165.63	39.71	175.87	530.11	11104	0.76	668	9.9	314
2	<0.00	21.34	0.01	0.21	0.58	0.65	6.52	2.07	29.07	11.68	64.09	16.01	192.96	47.05	333.61	811.61	11590	1.02	783	101.6	318
3	<0.00	26.55	<0.00	0.34	1.09	0.78	10.11	3.62	44.55	20.54	101.99	25.39	299.88	71.44	322.55	811.81	11203	0.72	975	78.1	313
4	<0.00	16.94	0.04	0.39	1.37	0.55	8.07	2.81	37.85	16.49	91.88	22.95	264.26	63.31	203.54	758.32	11625	0.51	621	43.4	318
5	<0.07	24.56	0.06	0.39	1.06	0.60	7.01	2.39	36.42	13.60	75.64	18.67	217.86	54.42	380.79	966.98	12226	0.67	902	63.0	317
6	<0.00	25.79	0.05	1.06	2.11	0.64	9.17	3.32	42.40	19.01	94.36	23.27	260.63	61.21	318.52	741.27	11568	0.45	947	24.3	309
7	0.44	44.07	0.28	2.01	2.75	1.64	14.52	5.42	67.26	29.18	150.07	36.43	410.22	94.29	702.78	1065.78	10016	0.79	1621	21.9	312
8	0.02	19.35	0.04	0.39	0.68	0.55	8.17	3.46	44.71	19.07	96.07	24.21	290.13	68.29	233.49	778.48	11231	0.71	710	49.6	317
9	0.26	23.93	0.61	4.72	4.33	2.27	11.14	3.21	36.45	13.70	67.49	17.19	197.31	47.22	375.17	887.19	11087	1.00	879	5.1	315
10	<0.00	24.86	0.07	<0.28	1.61	0.73	7.94	3.08	38.82	17.13	88.74	22.14	258.89	62.48	419.92	1031.24	11465	0.63	913	–	318
11	0.07	18.15	0.04	<0.27	0.99	0.67	6.37	1.94	27.95	12.49	71.26	17.89	210.53	52.73	248.45	757.43	12013	0.82	666	–	317
12	<0.00	24.11	0.06	0.45	2.04	0.65	11.28	3.50	51.12	22.68	118.97	28.99	356.84	82.11	270.54	920.34	12333	0.41	885	53.6	313
13	<0.00	24.26	0.02	0.47	1.17	0.69	9.56	3.19	43.52	19.67	97.75	24.83	277.90	67.65	224.14	622.01	11558	0.63	891	51.6	313
14	0.03	22.16	0.02	0.60	1.07	0.52	7.98	2.62	33.76	14.05	79.87	20.05	224.06	51.66	215.15	519.76	11539	0.54	814	36.9	317
15	0.43	25.65	0.11	1.66	2.12	0.88	7.71	3.29	40.34	17.58	101.26	25.20	298.52	72.78	290.44	823.18	11485	–	–	15.5	Disconcordant
16	<0.00	18.04	0.03	0.46	0.60	0.38	7.22	2.17	31.47	12.54	64.26	16.48	187.94	43.74	147.47	421.17	11608	0.56	662	39.2	308
17	0.24	29.09	0.64	4.73	6.48	2.92	13.57	4.10	43.14	17.75	93.15	23.08	270.00	67.23	488.39	1065.78	11362	0.95	1069	6.2	310
18	0.05	17.49	0.11	1.10	1.25	0.76	6.77	2.46	27.64	12.14	66.21	16.20	213.31	52.20	166.33	501.04	10800	0.80	642	15.9	317
19	0.07	17.89	0.08	0.35	0.92	0.48	6.32	2.81	29.53	13.85	72.14	18.84	215.90	52.31	258.11	823.73	11630	0.61	656	51.1	312
20	0.01	21.15	0.01	0.62	1.40	0.59	8.79	3.34	44.11	18.20	103.60	25.77	298.00	70.41	273.10	862.99	11596	0.51	776	34.1	313
21	0.38	27.90	0.21	1.68	2.62	0.77	8.70	3.62	44.10	17.00	89.39	20.93	242.26	53.30	197.34	479.12	10843	0.49	1025	16.6	315
22	<0.00	21.19	0.01	0.35	1.17	0.59	7.56	2.51	35.75	16.65	87.63	21.61	259.30	63.40	309.44	843.71	11063	0.61	778	60.5	314
23	5.03	37.63	0.88	3.80	1.82	0.70	11.08	3.20	41.03	17.91	90.78	22.97	257.36	60.36	303.09	678.73	11106	0.48	1384	9.9	315
24	0.74	32.73	2.11	12.81	11.82	5.43	26.91	7.33	66.91	23.60	113.17	27.48	317.15	74.65	278.31	653.85	10258	0.93	1203	2.6	313
25	0.07	23.88	0.05	0.58	1.07	0.65	7.67	2.85	40.75	18.32	97.38	24.58	283.57	71.54	267.87	725.51	11521	0.69	877	41.2	312
26	0.08	28.23	0.23	2.43	3.51	1.51	13.81	3.63	44.66	19.60	97.33	23.71	267.37	62.42	337.91	787.84	9660	0.66	1037	11.6	311
27	0.04	21.53	<0.00	0.69	0.69	0.57	7.21	2.62	35.90	14.89	87.85	23.75	277.46	68.73	209.24	596.56	11653	0.78	790	31.2	306
28	0.01	23.07	0.02	0.84	0.74	0.54	7.23	2.71	35.20	16.50	86.59	23.06	291.96	74.35	227.67	692.09	10579	0.71	847	27.5	304
29	0.06	21.72	0.01	0.21	1.36	0.67	5.89	2.64	33.19	14.86	81.68	21.02	250.09	62.19	258.22	646.94	11502	0.72	797	103.4	312
30	0.03	26.59	0.03	1.08	1.22	0.57	8.15	2.69	35.30	14.64	80.86	21.36	237.90	60.16	329.39	756.86	11737	0.55	977	24.6	316
whole-rock	14.20	31.30	4.15	18.40	4.02	0.74	3.08	0.52	2.73	0.51	1.23	0.22	1.58	0.21	14.00	4.08					

Note: $Eu_N/Eu^*_N = Eu_N/(Sm_N{*}Gd_N)^{1/2}$, where the subscript N stands for chondrite-normalized ratios; Ce^{4+}/Ce^{3+} ratios are calculated following the procedure of Ballard et al. (2002); Apparent age represent $^{206}Pb/^{238}U$ age; – Unavailable data of calculations.

U–Pb age data by Seltmann et al. (2011) and our new results, we can divide the felsic magmatism spatially associated with mineralization at Kalmakyr into two episodes, i.e., 330–324 Ma and 316–304 Ma (Fig. 11). The first episode of ore-related magmatism during 330–324 Ma had also been detected by SHRIMP U–Pb dating in Seltmann et al. (2011) from the Almalyk district, i.e., Sample 406801 from the Kara-Kiya granite (two of five analyzed zircon grains gave ages of 326.3 ± 4.7 Ma and 330.4 ± 4.7 Ma, respectively), and unpublished zircon LA-ICP-MS U–Pb age data of 326.1 ± 3.4 Ma (MSWD = 0.08, N = 16) for quartz monzonite from

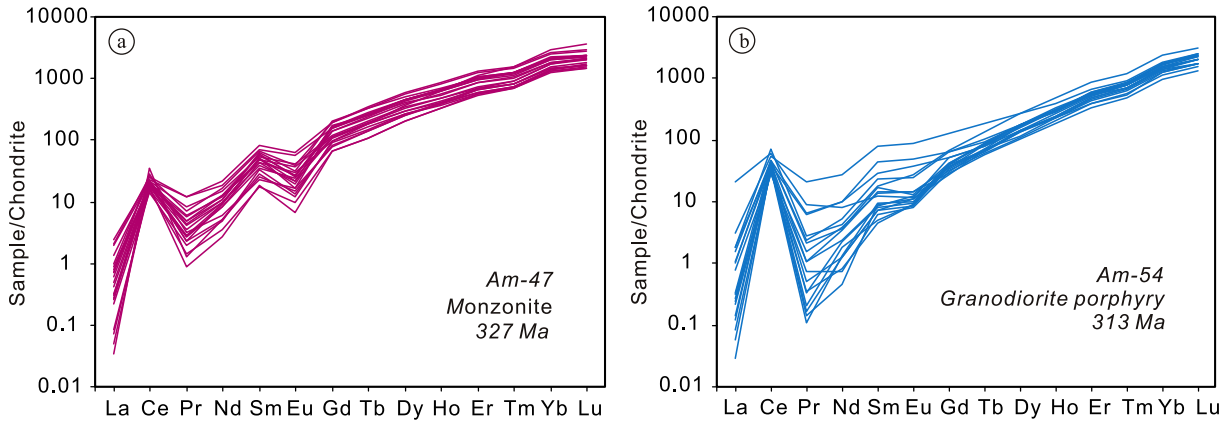

Fig. 8. Chondrite-normalized REE patterns of monzonite (a) and granodiorite porphyry (b) from the Kalmakyr deposit. Chondrite values are from Sun and McDonough (1989).

Table 4
In-situ Lu–Hf isotope analysis results of zircon of magmatic rocks from the Kalmakyr deposit.

Spot	Age[a](Ma)	$^{176}Yb/^{177}Hf$	2σ	$^{176}Lu/^{177}Hf$	2σ	$^{176}Hf/^{177}Hf$	2σ	$\varepsilon_{Hf}(0)$	$\varepsilon_{Hf}(t)$	T_{DM}(Ma)	T^{C}_{DM}(Ma)	$f_{Lu/Hf}$
Sample 47 (ore-hosting monzonite)												
AM-47-01	343	0.013722	0.000041	0.000573	0.000002	0.282610	0.000022	−5.7	1.7	900	1243	−0.98
AM-47-02	302	0.024702	0.000239	0.001019	0.000008	0.282758	0.000022	−0.5	5.9	701	940	−0.97
AM-47-03	339	0.045937	0.000550	0.001797	0.000016	0.282885	0.000027	4.0	11.0	532	641	−0.95
AM-47-04	340	0.026504	0.000902	0.001047	0.000036	0.282729	0.000020	−1.5	5.7	743	983	−0.97
AM-47-05	337	0.022163	0.000088	0.000893	0.000003	0.282696	0.000021	−2.7	4.5	786	1057	−0.97
AM-47-06	340	0.030535	0.000239	0.001218	0.000009	0.282695	0.000022	−2.7	4.5	794	1062	−0.96
AM-47-07	334	0.020112	0.000179	0.000851	0.000007	0.282786	0.000022	0.5	7.6	659	855	−0.97
AM-47-08	335	0.037060	0.000381	0.001449	0.000015	0.282693	0.000027	−2.8	4.2	802	1073	−0.96
AM-47-09	287	0.015368	0.000108	0.000645	0.000004	0.282669	0.000021	−3.6	2.5	819	1145	−0.98
AM-47-10	332	0.030585	0.000503	0.001227	0.000020	0.282791	0.000024	0.7	7.7	658	850	−0.96
AM-47-11	333	0.023342	0.000158	0.000933	0.000006	0.282707	0.000021	−2.3	4.8	772	1035	−0.97
AM-47-12	320	0.035375	0.000169	0.001389	0.000008	0.282780	0.000027	0.3	7.0	677	884	−0.96
AM-47-13	343	0.040706	0.000082	0.001786	0.000002	0.282703	0.000020	−2.4	4.7	795	1051	−0.95
AM-47-14	345	0.024237	0.000753	0.000940	0.000028	0.282641	0.000028	−4.6	2.7	865	1177	−0.97
AM-47-15	319	0.021515	0.000117	0.000839	0.000005	0.282683	0.000031	−3.1	3.7	803	1096	−0.97
Sample Am-54 (ore-bearing granodiorite porphyry)												
AM-54-01	314	0.016354	0.000052	0.000573	0.000002	0.282636	0.000022	−4.8	2.0	863	1202	−0.98
AM-54-02	318	0.016506	0.000180	0.001019	0.000008	0.282694	0.000018	−2.8	4.0	792	1075	−0.97
AM-54-03	313	0.025336	0.000101	0.001797	0.000016	0.282661	0.000022	−3.9	2.6	856	1162	−0.95
AM-54-04	318	0.017162	0.000032	0.001047	0.000036	0.282663	0.000018	−3.9	2.9	836	1145	−0.97
AM-54-05	317	0.018218	0.000041	0.000893	0.000003	0.282648	0.000021	−4.4	2.4	854	1178	−0.97
AM-54-06	309	0.018232	0.000209	0.001218	0.000009	0.282656	0.000022	−4.1	2.4	850	1168	−0.96
AM-54-07	312	0.025327	0.000189	0.000851	0.000007	0.282746	0.000026	−0.9	5.7	715	959	−0.97
AM-54-08	317	0.015598	0.000095	0.001449	0.000015	0.282585	0.000017	−6.6	0.0	956	1327	−0.96
AM-54-09	315	0.017657	0.000060	0.000645	0.000004	0.282647	0.000018	−4.4	2.4	850	1178	−0.98
AM-54-10	318	0.018938	0.000136	0.001227	0.000020	0.282545	0.000050	−8.0	−1.3	1007	1413	−0.96
AM-54-11	317	0.012579	0.000064	0.000933	0.000006	0.282530	0.000027	−8.6	−1.8	1021	1443	−0.97
AM-54-12	313	0.012165	0.000077	0.001389	0.000008	0.282672	0.000021	−3.5	3.1	831	1132	−0.96
AM-54-13	313	0.021030	0.000070	0.001786	0.000002	0.282663	0.000023	−3.9	2.7	853	1158	−0.95
AM-54-14	317	0.014518	0.000065	0.000940	0.000028	0.282608	0.000022	−5.8	1.0	911	1268	−0.97
AM-54-15	316	0.017384	0.000106	0.000839	0.000005	0.282669	0.000021	−3.6	3.1	823	1130	−0.97

[a] Apparent age represent $^{206}Pb/^{238}U$ age. $\varepsilon_{Hf}(t) = 10{,}000 \times (\{[(^{176}Hf/^{177}Hf)_S - (^{176}Lu/^{177}Hf)_S \times (e^{\lambda t} - 1)]/[(^{176}Hf/^{177}Hf)_{CHUR,\,0} - (^{176}Lu/^{177}Hf)_{CHUR} \times ((e^{\lambda t} - 1)] - 1\}$. $T_{DM} = 1/\lambda \times \ln\{1 + [(^{176}Hf/^{177}Hf)_S - (^{176}Hf/^{177}Hf)_{DM}]/[(^{176}Hf/^{177}Hf)_S - (^{176}Hf/^{177}Hf)_{DM}]\}$. $T^{C}_{DM} = T_{DM} - (T_{DM} - t) \times [(f_{cc} - f_s)/(f_{cc} - f_{DM})]$. $f_{Lu/Hf} = (^{176}Lu/^{177}Hf)_S/(^{176}Lu/^{177}Hf)_{CHUR} - 1$, where $\lambda = 1.867 \times 10^{-11}$/a (Söderlund et al., 2004); $(^{176}Lu/^{177}Hf)_S$ and $(^{176}Hf/^{177}Hf)_S$ are the measured values of the samples; $(^{176}Lu/^{177}Hf)_{CHUR} = 0.0332$ and $(^{176}Hf/^{177}Hf)_{CHUR,\,0} = 0.282772$ (Blichert-Toft and Albarède, 1997); $(^{176}Lu/^{177}Hf)_{DM} = 0.0384$ and $(^{176}Hf/^{177}Hf)_{DM} = 0.28325$ (Griffin et al., 2000); $(^{176}Lu/^{177}Hf)$mean crust = 0.015; fcc = $[(^{176}Lu/^{177}Hf)$ mean crust$/(^{176}Lu/^{177}Hf)_{CHUR}] - 1$; $f_s = f_{Lu/Hf}$; $f_{DM} = [(^{176}Lu/^{177}Hf)_{DM}/(^{176}Lu/^{177}Hf)_{CHUR}] - 1$; t = crystallization time of zircon.

the Kalmakyr deposit (Zhang Z.C., personal communication). The second episode of ore-related magmatism during 316–304 Ma from the Almalyk district has been certified by voluminous previous SHRIMP determination (Seltmann et al., 2011, 2014a,b; Dolgopolova et al., 2016).

Our newly obtained molybdenite Re–Os model ages (313.2 ± 7.2 Ma to 306.3 ± 4.3 Ma; Table 5) are significantly younger than the U–Pb age of the monzonite (327.2 ± 5.6 Ma; ore-hosting), and are relatively close to that of granodiorite porphyry (313.6 ± 2.8 Ma; ore-bearing). The Re–Os molybdenite model ages of two samples from the stage-1 quartz–molybdenite veinlets (313.2–312.2 Ma; Table 5) are notably similar to that of granodiorite porphyry, whereas the Re–Os model ages of five molybdenite samples from the stage-3 quartz–pyrite–chalcopyrite–molybdenite veinlets (310.4–306.3 Ma) are 3–7 Ma younger than that of granodiorite porphyry. The Re–Os isochron age of the stage-3 molybdenite (307.6 ± 2.5 Ma, Fig. 10a), similar to the weighted mean model age (308.6 ± 2.1 Ma, Fig. 10a), is also younger than the U–Pb age of the granodiorite porphyry. These results indicate that molybdenum mineralization occurred right after the emplacement of the granodiorite porphyry, as represented by the stage-1 molybdenite, but the major phase of

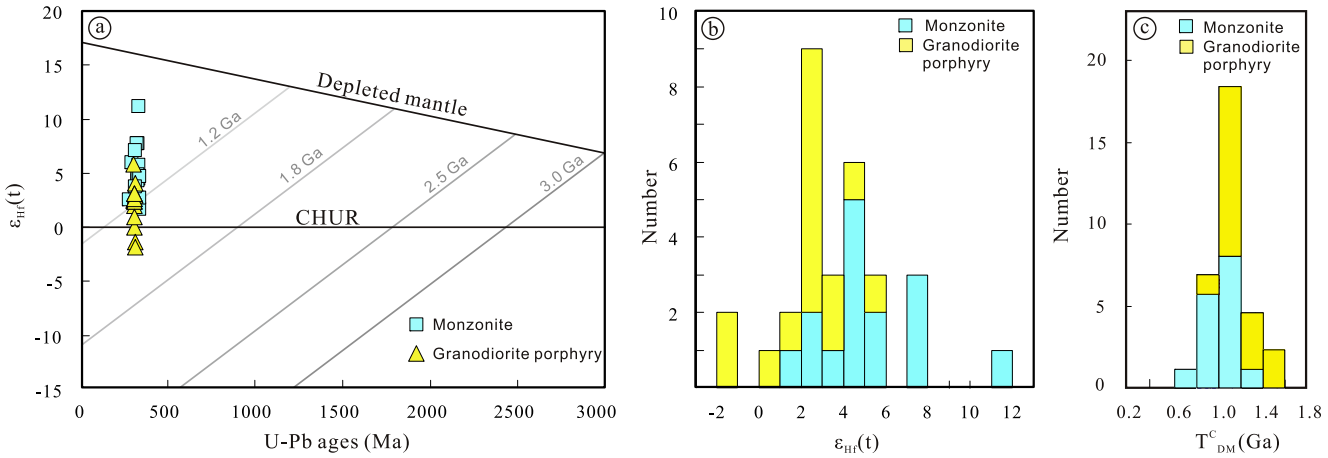

Fig. 9. a) $\varepsilon_{Hf}(t)$ versus U–Pb ages, b) histogram of $\varepsilon_{Hf}(t)$ values, and c) histogram of Hf crustal model ages (T^{C}_{DM}) of zircons from ore-related intrusive rocks of the Kalmakyr deposit. Depleted mantle evolution is calculated by using $\varepsilon_{Hf}(t) = 16.9$ at t = 0 Ma and $\varepsilon_{Hf}(t) = 6.4$ at t = 3.0 Ga. CHUR: chondrite uniform reservoir.

Table 5
Re–Os data for molybdenite samples of the Kalmakyr deposit.

Sample	Weight (g)	Re (ppm)		^{187}Re (ppm)		^{187}Os (ppb)		Model age (Ma)	
		Measured	±2σ	Measured	±2σ	Measured	±2σ	Measured	±2σ
Am-1	0.00306	135	1	85	1	439.3	4.1	309.3	5.0
Am-2	0.00324	98	1	62	1	319.5	3.2	310.4	5.2
AM-3	0.00928	899	18	565	11	2955	24	313.2	7.2
Am-9	0.00318	676	5	425	3	2175	19	306.3	4.3
Am-10	0.00296	774	6	487	4	2514	22	309.2	4.4
Am-11	0.00305	670	6	421	4	2197	21	312.2	4.7
Am-12	0.00301	865	8	544	5	2802	31	308.6	5.0

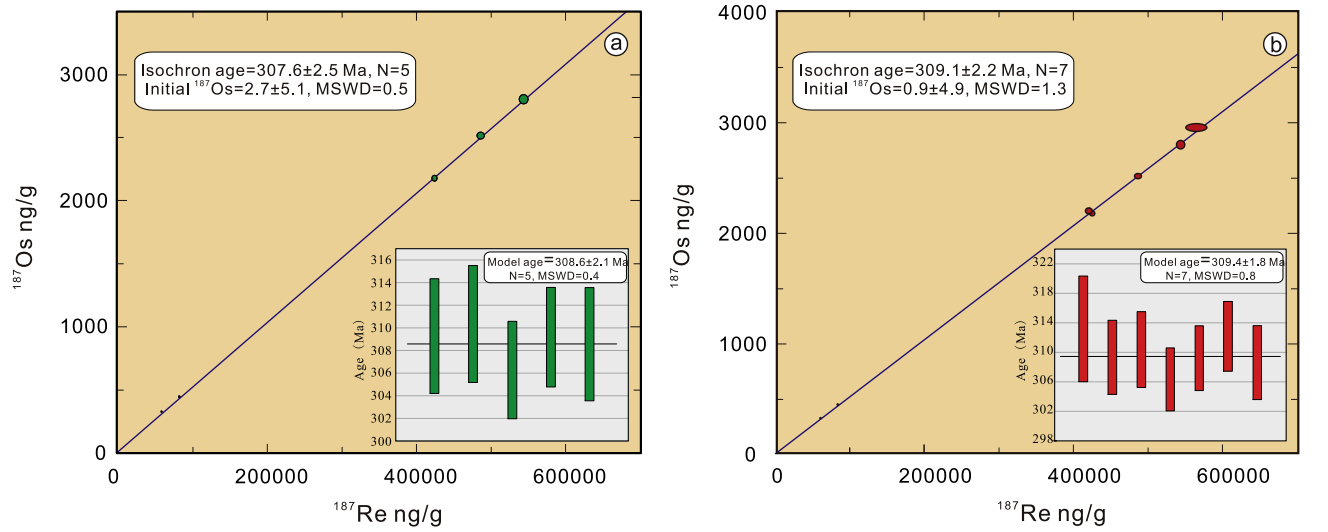

Fig. 10. a) Re–Os isochron and model age diagram showing data for stage-3 molybdenite samples, b) Re–Os isochron and model age diagram showing data for both stage-1 and stage-3 molybdenite samples.

mineralization, i.e., stage-3 veinlets, which account for 90% of the gold contained at Kalmakyr deposit (Golovanov et al., 2005), took place after significant cooling of the intrusion. However, we cannot rule out the possibility that another pulse of magmatic intrusion was emplaced simultaneously with the major phase of mineralization, as revealed by the age overlap of U–Pb dating of monzonite (308 ± 1 Ma and 308 ± 4 Ma; Seltmann et al. (2011)) and our Re–Os weighted mean model age of the stage-3 veinlets (308.6 ± 2.1 Ma) (Fig. 10a). In either case, the geochronological data indicate that the Kalmakyr deposit was formed from a long-lived magmatic hydrothermal mineralization system.

7.2. Sources and redox conditions of monzonite versus granodiorite porphyry

Previous studies have indicated that the ore-related magmatic rocks in the Almalyk district have typical subduction-related geochemical feature (Golovanov et al., 2005), and form part of the Devono-Carboniferous Beltau–Kurama magmatic arc related to the northward subduction of the Turkestan Ocean beneath the Middle Tien Shan (Seltmann et al., 2011; Turamuratov et al., 2011). Magmas forming the arc may have been derived from the upper mantle above the subduction zone, the lower crust, or both

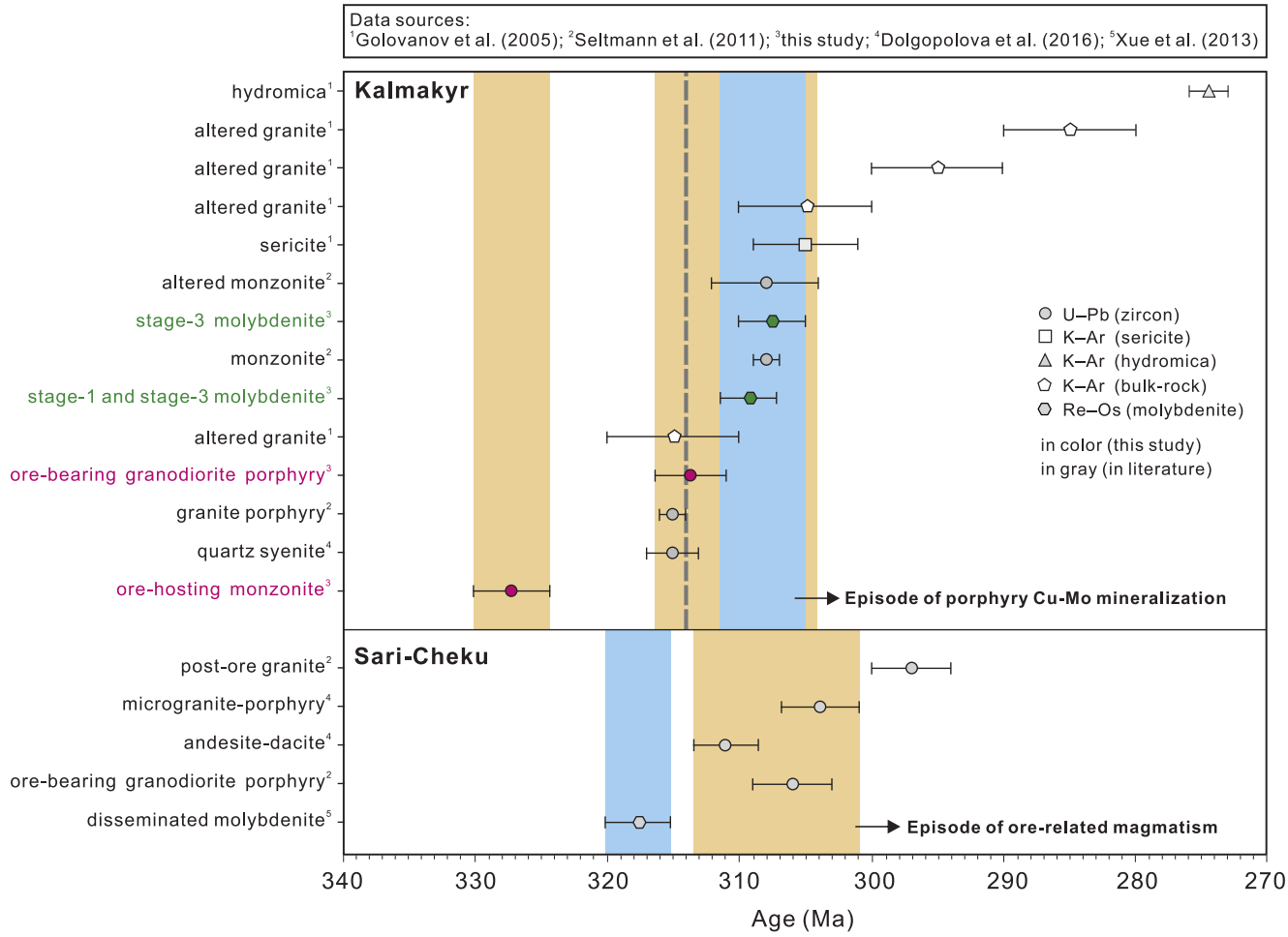

Fig. 11. Summary of geochronological data from the Kalmakyr deposit, Almalyk district. Error bars are 2σ. *Grey dashed line* represents preliminary Re–Os molybdenite age of 315 Ma in Seltmann et al. (2014b).

(Yakubchuk et al., 2002). In order to better understand the mineralization processes at Kalmakyr, it is worth examining the contributions from the mantle and the crust for the ore-hosting monzonite and the ore-bearing granodiorite porphyry. Also, it is known that oxidized magmas are relatively favorable for porphyry copper mineralization than reduced ones (Ballard et al., 2002; Hoskin and Schaltegger, 2003; Peytcheva et al., 2009; Sun et al., 2015), and so it is of interest to compare the monzonite and granodiorite porphyry in terms of redox conditions. Useful information on both magmatic sources and redox conditions may be derived from Lu–Hf isotopes and REE compositions of zircon and Re–Os isotopes of molybdenite, as discussed below.

Zircon grains from Kalmakyr monzonite and granodiorite porphyry exhibit generally similar chondrite-normalized REE patterns (Fig. 8), e.g., inclination to the left, positive Ce anomalies, and negative Eu anomalies, indicating that these rocks may have been derived from similar magmatic sources and may have experienced similar fractionation processes, as is also suggested by previous bulk-rock geochemical studies (Golovanov et al., 2005). However, subtle differences in REE patterns can be observed between monzonite and granodiorite porphyry (Fig. 8), especially in Ce and Eu anomalies. Previous experimental studies have shown that the Ce anomaly is directly related to the oxidation state of the magmas (Burnham and Berry, 2012; Trail et al., 2011, 2012). In the present study, the monzonite has an average Eu_N/Eu_N^* value of 0.33, and an average Ce^{4+}/Ce^3 value of 624, whereas the granodiorite porphyry has an average Eu_N/Eu_N^* value of 0.68, and an average Ce^{4+}/Ce^3 value of 890 (Table 3). As compared to La and Pr, the concentrations of Nd in zircon can be more accurately and precisely determined (Chelle-Michou et al., 2014); we therefore use the Ce/Nd ratio as a proxy for Ce anomaly to further investigate the redox conditions of ore-related magmas at Kalmakyr deposit. The zircon Ce/Nd values range from 1.3 to 12.4 (average 3.9) for the monzonite and from 2.6 to 103.4 (average 36.8) for the granodiorite porphyry (Table 3). These REE signatures suggest that the magma for the granodiorite porphyry is more oxidized than that for the monzonite.

The significant overlap in εHf (t) values between monzonite and granodiorite porphyry, mainly in the range of +1 to +6 (Fig. 9 a and b), and in T_{DM}^C ages, mainly from 1400 to 800 Ma (Fig. 9c), also indicates that these rocks were derived from similar magmatic sources, mainly in juvenile lower crust with variable crust contamination (Kinny and Maas, 2003). However, slight differences are also observed between the two intrusions. The monzonite has higher $\varepsilon_{Hf}(t)$ values (+1.7 to +11) and younger T_{DM}^C ages (1243 to 641 Ma) than the granodiorite porphyry ($\varepsilon_{Hf}(t) = -1.8$ to +5.7; T_{DM}^C ages = 1443 to 959 Ma) (Table 4). These differences suggest that there was a greater mantle contribution in the monzonite than in the granodiorite porphyry, and that a greater crustal components with elevated crustal model ages and decreased $\varepsilon_{Hf}(t)$ values was involved in the formation of the granodiorite magma.

A mantle contribution for the parental magmas of the Kalmakyr deposit is also supported by rhenium concentrations of molybdenite in this study. Mineral deposits involving mantle components

generally have higher rhenium concentrations than those derived from the crust (Stein et al., 2001). It was proposed that rhenium contents in molybdenite decrease from hundreds of ppm for mantle sources, through tens of ppm for mixed mantle and crustal sources, to several ppm for crustal sources (Mao et al., 1999). The rhenium concentrations of molybdenite from the Kalmakyr deposit range from 98 to 899 ppm (Table 5), with an average of 590 ppm, suggesting a major mantle contribution for rhenium and by inference the ore metals.

7.3. A model for the ore-forming processes of the Kalmakyr porphyry deposit

The new geochronological and geochemical data obtained in this study, together with the regional database on late Paleozoic magmatism and metallogeny in the Tien Shan (Biske et al., 2013; Konopelko et al., 2009; Seltmann et al., 2011), can be used to place the Kalmakyr deposit in the regional geodynamic framework. Continued northward subduction of the Turkestan Ocean beneath the Middle Tien Shan led to voluminous Carboniferous to Permian subduction-related magmatism, forming the Beltau–Kurama magmatic arc (Chernyshev et al., 2011; Golovanov et al., 2005; Seltmann et al., 2011). This belt hosts major porphyry Cu–Au–Mo and epithermal Au deposits around the Kurama range (Fig. 2), generally considered as a southern active continental margin of the Kazakhstan continent (Yakubchuk et al., 2002). The final closure of the Turkestan Ocean is believed to have commenced in the Late Carboniferous (~320 Ma) and continued into the Early Permian (295–290 Ma) (Biske and Seltmann, 2010). Our zircon U–Pb ages of the ore-related intrusive rocks (327–314 Ma) and molybdenite Re–Os age (313–306 Ma) indicate that in the Kalmakyr deposit the parental magmas were emplaced in a late Carboniferous mature magmatic arc setting in relation to the latest subduction process of the Turkestan Ocean.

Although our age data indicate that the monzonite predated mineralization by at least 16 m.y., and thus its emplacement is not directly related to the formation of the Kalmakyr deposit, it is notable that the majority of the orebodies are hosted by monzonite (Fig. 2). The monzonite and granodiorite porphyry belong to the same intrusive complex, which appears to be controlled by the intersection between NW-trending deep-seated faults and the EW-trending Kalmakyr fault (Fig. 2). Furthermore, the overall similarity in geochemistry between monzonite and granodiorite porphyry, as discussed above, suggests that the rocks were rooted in a common source region. The evolution of this integrated magmatic–hydrothermal system is postulated below and portrayed in Fig. 12.

A magma chamber was developed in the mid-lower crust underneath the Kalmakyr deposit from 330 to 324 Ma, with the magma being sourced from the lower crust and the upper mantle (Fig. 12a), where partial melting may have been facilitated by volatiles from the subduction zone below. At about 327 Ma, some magma from this magma chamber intruded into the Devonian vol-

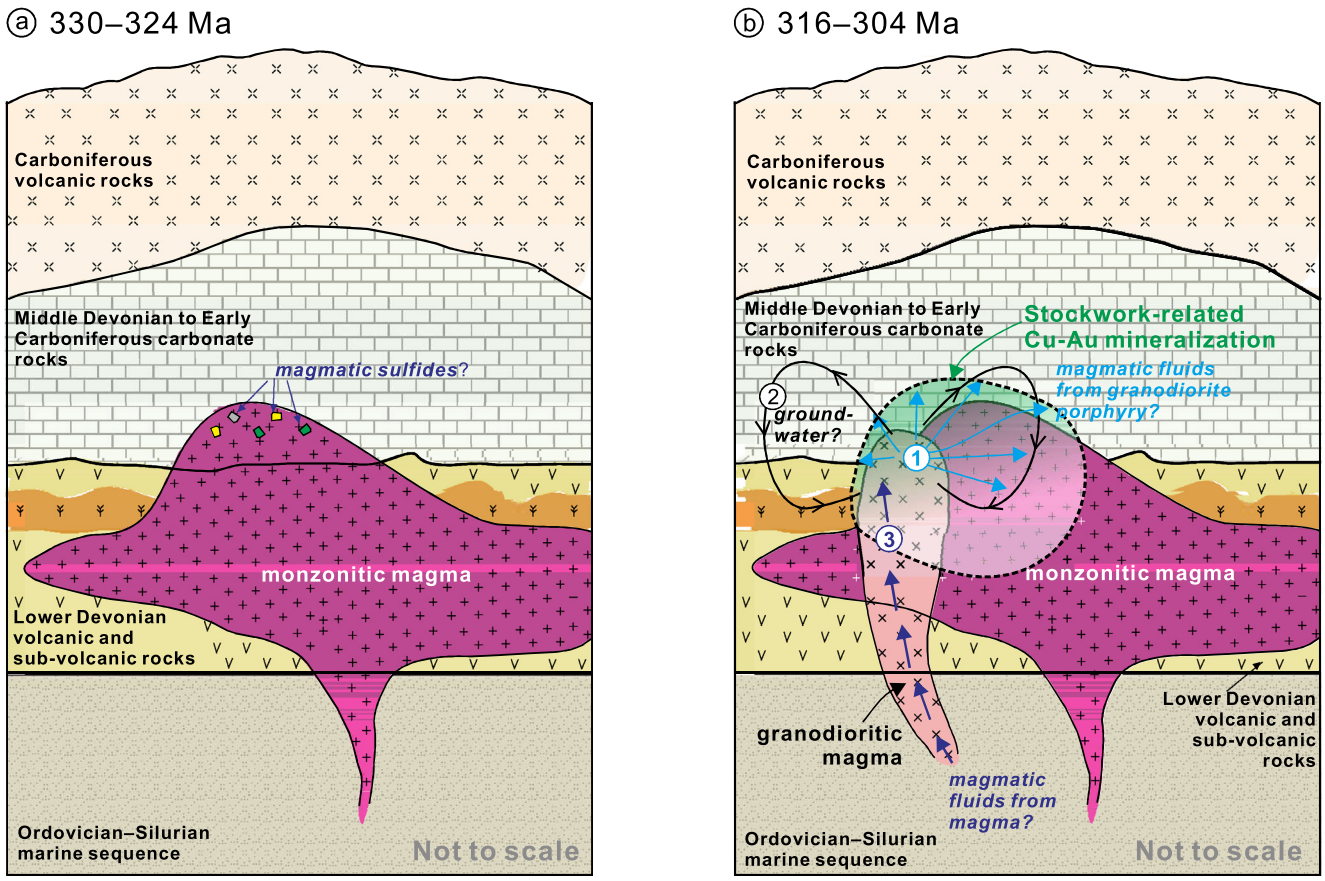

Fig. 12. Cartoons showing the evolution of felsic magmas and associated porphyry Cu–Au mineralization at Kalmakyr deposit. a) injection of volatile-rich and metal-rich mafic melts from the upper mantle and the subduction zone below into a thickened juvenile crust triggered partial melting and development of a magma chamber (330–324 Ma); monzonite was emplaced at ~327 Ma with no major mineralization, partly due to its relatively reducing conditions. b) granodiorite porphyry (but more evolved) was emplaced at ~314 Ma (magmatic activity may have lasted from 316 to 304 Ma), followed by mineralization (represented by stage-1 molybdenite, marked by circled 1), thermal convection of groundwater (marked by circled 2), and probably metal-rich fluid flow the magma chamber (marked by circled 3); these late fluids may have remobilized ore elements dispersed in the monzonite and granodiorite porphyry, and precipitated them in the mineralization zones.

canic and carbonates rocks at the Kalmakyr area, forming the monzonite (Fig. 12a). At this time, the magma was relatively reducing, as discussed above, and probably relatively volatile-poor, and so no major mineralization took place. As compatible elements, Cu and Au may have been dispersed in trace magmatic sulfides before fluid saturation (partly due to relatively reducing conditions), whereas as an incompatible element, molybdenum may not have been enriched in the magma.

By about 314 Ma, with more and more volatiles supplied from the subduction zone, a second batch of magma intruded the Kalmakyr area forming the granodiorite intrusion (Fig. 12b). The increased contents of volatiles, and elevated oxygen fugacity (possibly due to incorporation of subduction zone-derived volatiles), favors partitioning of copper and gold into the magmatic fluids following the emplacement of the granodiorite porphyry (Jugo, 2009; Lee et al., 2012). In addition to the Ce and Eu anomalies διστυσ σεδ above, the increase in oxygen fugacity in the ore-forming fluids associated with the granodiorite porphyry is also reflected by the development of abundant anhydrite veinlets in the mineralized zones and magnetite and hematite associated with quartz–sericite alteration (Golovanov et al., 2005; Mathur et al., 2000; Sun et al., 2013, 2015). Molybdeum and copper sulfides and gold were precipitated due to temperature drop and fluid-rock interaction (alterations) which resulted in decrease in oxygen fugacity.

The Re–Os model ages of stage-3 molybdenite suggest that mineralization event at Kalmakyr may have lasted for up to 7 m.y. after emplacement of the granodiorite porphyry. It might be possible that in the late stage of mineralization, the mineralizing fluids were not magmatic fluids derived from the granodiorite intrusion, but rather groundwater driven by thermal convection related to the heat anomaly caused by the intrusion (Fig. 12b). The groundwater may have remobilized ore elements dispersed in the monzonite, as well as the granodiorite porphyry, and precipitated them in the mineralization zones (Fig. 12b). Alternatively, magmatic fluids may have been released directly from the magma chamber after emplacement of the granodiorite porphyry, adding more ore metals to the mineralization zones. In the latter case, the granodiorite porphyry does not represent the parent magma of the mineralizing fluids; rather, the granodiorite porphyry and the mineralizing fluids were brothers from the same parent, i.e., the deeply seated magma chamber. In summary, our geochronological data of zircon and molybdenite indicate that the Kalmakyr deposit formed from a long-lived magmatic-hydrothermal system. This system was favorably located in a structural framework connected with fertile magmatic sources above the subduction zone, and was furnished with volatiles from the subducting plate and metals from the upper mantle.

8. Conclusions

(1) The Kalmakyr porphyry deposit is spatially associated with middle to late Carboniferous subduction-related monzonite and granodiorite porphyry intrusions. The Copper–gold–molybdenum mineralization occurs as stockworks, veinlets and disseminations of chalcopyrite, pyrite and molybdenite, mainly in the phyllic and K-silicate alteration zones developed in the monzonite, close to the granodiorite porphyry.

(2) U–Pb ages of zircon grains from ore-hosting monzonite and ore-bearing granodiorite porphyry are 327.2 ± 5.6 Ma and 313.6 ± 2.8 Ma, respectively, whereas molybdenite from stockwork and veinlet ores shows Re–Os model ages from 313.2 to 306.3 Ma. These data indicate that the mineralization post-dated the monzonite by 14 m.y., starting right after the emplacement of the granodiorite porphyry, and lasting for some 7 m.y.

(3) The ore-related magmas in the Kalmakyr deposit were derived from partial melting of a thickened lower crust with input of mantle components and variable crust contamination, resulting in zircon $\varepsilon_{Hf}(t)$ values mainly in the range of +1 to +6. The high rhenium concentrations (98–899 ppm) of molybdenite also indicate its major mantle contribution and by inference ore metals.

(4) When monzonite was emplaced, the oxygen fugacity and volatile contents in the magma chamber were relatively low; ore metals might disperse in the intrusive rock and no major mineralization took place. By the time granodiorite porphyry was emplaced, the oxygen fugacity and volatile contents in the magma chamber were increased, favoring copper and gold enrichment in the magmatic fluids. Following the mineralization associated with magmatic fluids released from the granodiorite porphyry, groundwater convection may have remobilized ore metals previously dispersed in the monzonite and contributed to mineralization. Prolonged hydrothermal activities may have also been contributed by fluids, directly derived from the magma chamber. The Kalmakyr deposit formed from a long-lived magmatic-hydrothermal system connected with fertile magmatic sources in relation to the subduction of the Turkestan Ocean beneath the Middle Tien Shan.

Acknowledgements

This manuscript greatly benefited from constructive reviews by Alexander Yakubchuk and anonymous reviewers. We express our appreciation to Zhaochong Zhang for collaboration with this study, and to Arpay H. Turesebekov and Obidjon Kodirov and the staff of Almalyk Mining and Metallugical Complex for site access and help during the field work. We thank Dr. Andao Du for helping with the acquisition of the molybdenite Re–Os age dating and Dr. Mengning Dai for assistance in the zircon U–Pb isotope dating, trace elements and Hf isotopes analyses. This study was sponsored by the National Natural Science Foundation of China (U1303292, 41602076).

References

Andersen, T., 2002. Correction of common lead in U-Pb analyses that do not report ^{204}Pb. Chem. Geol. 192, 59–79.
Bakirov, A., Tagiri, M., Sakiev, K., Ivleva, E., 2003. The Lower Precambrian rocks in the Tien Shan and their geodynamic setting. Geotectonics 37, 368–380.
Ballard, J.R., Palin, J.M., Campbell, I.H., 2002. Relative oxidation states of magmas inferred from Ce(IV)/Ce(III) in zircon: application to porphyry copper deposits of northern Chile. Contrib. Miner. Petrol. 144, 347–364.
Belousova, E., Griffin, W.L., O'reilly, S.Y., Fisher, N., 2002. Igneous zircon: trace element composition as an indicator of source rock type. Contrib. Miner. Petrol. 143, 602–622.
Biske, Y.S., Seltmann, R., 2010. Paleozoic Tian-Shan as a transitional region between the Rheic and Urals-Turkestan oceans. Gondwana Res. 17, 602–613.
Biske, Y.S., Konopelko, D.L., Seltmann, R., 2013. Geodynamics of late Paleozoic magmatism in the Tien Shan and its framework. Geotectonics 47, 291–309.
Blichert-Toft, J., Albarède, F., 1997. The Lu-Hf isotope geochemistry of chondrites and the evolution of the mantle-crust system. Earth Planet. Sci. Lett. 148 (1–2), 243–258.
Burnham, A.D., Berry, A.J., 2012. An experimental study of trace element partitioning between zircon andmelt as a function of oxygen fugacity. Geochim. Cosmochim. Acta 95, 196–212.
Chelle-Michou, C., Chiaradia, M., Ovtcharova, M., Ulianov, A., Wotzlaw, J.F., 2014. Zircon petrochronology reveals the temporal link between porphyry systems and the magmatic evolution of their hidden plutonic roots (the Eocene Coroccohuayco deposit, Peru). Lithos 198, 129–140.
Chernyshev, I.V., Kovalenker, V.A., Goltsman, Y.V., Plotinskaya, O.Y., Bairova, E.D., Oleinikova, T.I., 2011. Rb-Sr isochron dating of Late Paleozoic epithermal ore-forming processes: a case study of the Kairagach gold deposit, Kurama ore district, Central Tien Shan. Geochem. Int. 49, 107–119.
Chiaradia, M., Schaltegger, U., Spikings, R., Wotzlaw, J.F., Ovtcharova, M., 2013. How accurately can we date the duration of magmatic-hydrothermal events in porphyry systems? An invited paper. Econ. Geol. 108, 565–584.

Chu, N.C., Taylor, R.N., Chavagnac, V., Nesbitt, R.W., Boella, R.M., Milton, J.A., German, C.R., Bayon, G., Burton, K., 2002. Hf isotope ratio analysis using multi-collector inductively coupled plasma mass spectrometry: an evaluation of isobaric interference corrections. J. Anal. At. Spectrom. 17, 1567–1574.
Cooke, D.R., Hollings, P., Walshe, J.L., 2005. Giant porphyry deposits: characteristics, distribution, and tectonic controls. Econ. Geol. 100, 801–818.
De Bievre, P., Taylor, P., 1993. Table of the isotopic compositions of the elements. Int. J. Mass Spectrom. Ion Processes 123, 149–166.
Dolgopolova, A., Seltmann, R., Konopelko, D., Biske, Yu.S., Shatov, V., Armstrong, R., Belousova, E., Pankhurst, R., Koneev, R., Divaev, F., 2016. Geodynamic evolution of the western Tien Shan, Uzbekistan: insights from U-Pb SHRIMP geochronology and Sr-Nd-Pb-Hf isotope mapping of granitoids. Gondwana Res. http://dx.doi.org/10.1016/j.gr.2016.10.022.
Du, A., Wu, S., Sun, D., Wang, S., Qu, W., Markey, R., Stain, H., Morgan, J., Malinovskiy, D., 2004. Preparation and certification of Re-Os dating reference materials: molybdenites HLP and JDC. Geostand. Geoanal. Res. 28, 41–52.
Elhlou, S., Belousova, E., Griffin, W., Pearson, N., O'reilly, S., 2006. Trace element and isotopic composition of GJ-red zircon standard by laser ablation. Geochim. Cosmochim. Acta 70, A158.
Golovanov, I.M., Seltmann, R., Kremenetsky, A.A., 2005. The porphyry Cu–Au/Mo deposits of Central Euroasia: 2. The Almalyk (Kalmakyr–Dalnee) and Saukbulak Cu–Au porphyra systems, Uzbekistan. In: Porter, T.M. (Ed.), Super Porphyry Copper and Gold Deposits: A Global Perspective, vol. 2. PGC Publishing, Adelaide, pp. 513–523.
Goolaerts, A., Mattielli, N., de Jong, J., Weis, D., Scoates, J.S., 2004. Hf and Lu isotopic reference values for the zircon standard 91500 by MC-ICP-MS. Chem. Geol. 206, 1–9.
Griffin, W.L., Pearson, N.J., Belousova, E., Jackson, S.E., Van Achterbergh, E., O'Reilly, S.Y., Shee, S.R., 2000. The Hf isotope composition of cratonic mantle: LAM-MC-ICPMS analysis of zircon megacrysts in kimberlites. Geochim. Cosmochim. Acta 64 (1), 133–147.
Griffin, W., Wang, X., Jackson, S., Pearson, N., O'Reilly, S.Y., Xu, X., Zhou, X., 2002. Zircon chemistry and magma mixing, SE China: in-situ analysis of Hf isotopes, Tonglu and Pingtan igneous complexes. Lithos 61, 237–269.
Han, B.F., He, G.Q., Wang, X.C., Guo, Z.J., 2011. Late Carboniferous collision between the Tarim and Kazakhstan-Yili terranes in the western segment of the South Tian Shan Orogen, Central Asia, and implications for the Northern Xinjiang, western China. Earth Sci. Rev. 109, 74–93.
Hoskin, P.W., Ireland, T.R., 2000. Rare earth element chemistry of zircon and its use as a provenance indicator. Geology 28, 627–630.
Hoskin, P.W., Schaltegger, U., 2003. The composition of zircon and igneous and metamorphic petrogenesis. Rev. Mineral. Geochem. 53, 27–62.
Jahn, B.M., Wu, F., Chen, B., 2000. Granitoids of the Central Asian Orogenic Belt and continental growth in the Phanerozoic. Geol. Soc. Am. Spec. Pap. 350, 181–193.
Jugo, P.J., 2009. Sulfur content at sulfide saturation in oxidized magmas. Geology 37, 415–418.
Kinny, P.D., Maas, R., 2003. Lu–Hf and Sm–Nd isotope systems in zircon. Rev. Mineral. Geochem. 53, 327–341.
Konopelko, D., Biske, G., Seltmann, R., Eklund, O., Belyatsky, B., 2007. Hercynian post-collisional A-type granites of the Kokshaal Range, Southern Tien Shan, Kyrgyzstan. Lithos 97, 140–160.
Konopelko, D., Biske, G., Seltmann, R., Kiseleva, M., Matukov, D., Sergeev, S., 2008. Deciphering Caledonian events: timing and geochemistry of the Caledonian magmatic arc in the Kyrgyz Tien Shan. J. Asian Earth Sci. 32, 131–141.
Konopelko, D., Seltmann, R., Biske, G., Lepekhina, E., Sergeev, S., 2009. Possible source dichotomy of contemporaneous post-collisional barren I-type versus tin-bearing A-type granites, lying on opposite sides of the South Tien Shan suture. Ore Geol. Rev. 35, 206–216.
Konopelko, D., Kullerud, K., Apayarov, F., Sakiev, K., Baruleva, O., Ravna, E., Lepekhina, E., 2012. SHRIMP zircon chronology of HP-UHP rocks of the Makbal metamorphic complex in the Northern Tien Shan, Kyrgyzstan. Gondwana Res. 22, 300–309.
Lee, J.K., Williams, I.S., Ellis, D.J., 1997. Pb, U and Th diffusion in natural zircon. Nature 390, 159–162.
Lee, C.T.A., Luffi, P., Chin, E.J., Bouchet, R., Dasgupta, R., Morton, D.M., Le Roux, V., Yin, Q.-Z., Jin, D., 2012. Copper systematics in arc magmas and implications for crust-mantle differentiation. Science 336, 64–68.
Lomize, M., Demina, L., Zarshchikov, A., 1997. The Kyrgyz-Terskei Paleoceanic Basin, Tien Shan. Geotectonics 31, 463–482.
Ludwig, K.R., 2003. User's manual for Isoplot 3.00: a geochronological toolkit for Microsoft Excel. Kenneth R. Ludwig.
Mao, J., Zhang, Z., Zhang, Z., Du, A., 1999. Re–Os isotopic dating of molybdenites in the Xiaoliugou W (Mo) deposit in the northern Qilian mountains and its geological significance. Geochim. Cosmochim. Acta 63, 1815–1818.
Mao, J., Pirajno, F., Lehmann, B., Luo, M., Berzina, A., 2014. Distribution of porphyry deposits in the Eurasian continent and their corresponding tectonic settings. J. Asian Earth Sci. 79, 576–584.
Mathur, R., Ruiz, J., Titley, S., Gibbins, S., Margotomo, W., 2000. Different crustal sources for Au-rich and Au-poor ores of the Grasberg Cu–Au porphyry deposit. Earth Planet. Sci. Lett. 183, 7–14.
Meshchaninov, Y.Z., Azin, V.N., 1973. Distribution of gold in a copper porphyry deposit, Almalyk region. Int. Geol. Rev. 6, 660–663.
Pašava, J., Vymazalová, A., Košler, J., Koneev, R.I., Jukov, A.V., Khalmatov, R.A., 2010. Platinum-group elements in ores from the Kalmakyr porphyry Cu–Au–Mo deposit, Uzbekistan: bulk geochemical and laser ablation ICP-MS data. Miner. Deposita 45, 411–418.
Peytcheva, I., von Quadt, A., Neubauer, F., Frank, M., Nedialkov, R., Heinrich, C., Strashimirov, S., 2009. U-Pb dating, Hf-isotope characteristics and trace-REE-patterns of zircons from Medet porphyry copper deposit, Bulgaria: implications for timing, duration and sources of ore-bearing magmatism. Mineral. Petrol. 96, 19–41.
Porter, T.M., 2006. The Tien Shan Belt: Golden Heart of Central Asia. Gangue 88.
Rubatto, D., 2002. Zircon trace element geochemistry: partitioning with garnet and the link between U-Pb ages and metamorphism. Chem. Geol. 184, 123–138.
Samonov, I.Z., Pozharisky, I.F., 1977. Deposits of copper. In: Smirnov, V.I. (Ed.), Ore Deposits of the USSR, vol. 2. Pitman Publishing, pp. 106–181.
Scherer, E., Münker, C., Mezger, K., 2001. Calibration of the lutetium-hafnium clock. Science 293, 683–687.
Seltmann, R., Porter, T.M., 2005. The porphyry Cu-Au/Mo deposits of central Eurasia: tectonic, geologic, and metallogenic setting and significant deposits. In: Porter, T.M. (Ed.), Super Porphyry Copper and Gold Deposits: A Global Perspective, vol. 2. PGC Publishing, Adelaide, pp. 467–512.
Seltmann, R., Konopelko, D., Biske, G., Divaev, F., Sergeev, S., 2011. Hercynian post-collisional magmatism in the context of Paleozoic magmatic evolution of the Tien Shan orogenic belt. J. Asian Earth Sci. 42, 821–838.
Seltmann, R., Porter, T.M., Pirajno, F., 2014a. Geodynamics and metallogeny of the central Eurasian porphyry and related epithermal mineral systems: a review. J. Asian Earth Sci. 79, 810–841.
Seltmann, R., Koneev, R., Divaev, F.K., Khalmatov, R.A., 2014b. New data on the absolute age of magmatism and gold mineralization in Uzbekistan. Geol. Miner. Res. 2, 10–15 (In Russian).
Sengör, A., Natal'In, B., Burtman, V., 1993. Evolution of the Altaid tectonic collage and Palaeozoic crustal growth in Eurasia. Nature 364, 299–307.
Shayakubov, T., Islamov, F., Golovanov, I., Kashirsky, S., Kremenetsky, A., Minzer, E., 1999. Almalyk and Saukbulak Ore fields. In: Shayakubov, T., Islamov, F., Kremenetsky, A., Seltmann, R. (Eds.), Au, Ag, and Cu Deposits of Uzbekistan. Excursion Guidebook, IGCP 373 Publication No 11. GeoForschungsZentrum Potsdam, pp. 75–90.
Smoliar, M.I., Walker, R.J., Morgan, J.W., 1996. Re–Os ages of group IIA, IIIA, IVA, and IVB iron meteorites. Science 271, 1099–1102.
Söderlund, U., Patchett, P.J., Vervoort, J.D., Isachsen, C.E., 2004. The 176 Lu decay constant determined by Lu–Hf and U-Pb isotope systematics of Precambrian mafic intrusions. Earth Planet. Sci. Lett. 219 (3), 311–324.
Sokolov, A.L., 1995. The regional and local controls on giant-scale copper and gold mineralisation, Uzbekistan. In: Clark, A.H. (Ed.), Giant Ore Deposits II. Controls on the Scale of Orogenic Magmatic-Hydrothermal Mineralisation. Proceedings of the Second Giant Ore Deposits Workshop, Kingston, Ontario, Canada, April 25-27, 1995. Department of Geological Sciences, Queens University, Kingston Ontario, pp. 450–474.
Stein, H., Markey, R., Morgan, J., Hannah, J., Scherstén, A., 2001. The remarkable Re–Os chronometer in molybdenite: how and why it works. Terra Nova 13, 479–486.
Sun, S.S., McDonough, W.F., 1989. Chemical and isotopic systematics of oceanic basalts: implications for mantle composition and processes. Geol. Soc., London, Spec. Publ. 42, 313–345.
Sun, W.D., Liang, H.Y., Ling, M.X., Zhan, M.Z., Ding, X., Zhang, H., Yang, X.Y., Li, L.L., Ireland, T.R., Wei, Q.R., Fan, W.M., 2013. The link between reduced porphyry copper deposits and oxidized magmas. Geochim. Cosmochim. Acta 103, 263–275.
Sun, W.D., Huang, R.F., Li, H., Hu, Y.B., Zhang, C.C., Sun, S.J., Zhang, L.P., Ding, X., Li, C. Y., Zartman, R.E., Ling, M.X., 2015. Porphyry deposits and oxidized magmas. Ore Geol. Rev. 65, 97–131.
Trail, D., Watson, E.B., Tailby, N.D., 2011. The oxidation state of Hadean magmas and implications for early Earth's atmosphere. Nature 480, 79–82.
Trail, D., Watson, E.B., Tailby, N.D., 2012. Ce and Eu anomalies in zircon as proxies for the oxidation state of magmas. Geochim. Cosmochim. Acta 97, 70–87.
Turamuratov, I.B., Isokov, M.U., Hodjaev, N.T., Abduazimova, Z.M., Zimalina, V.Y., Tsoy, V.D., Krikunova, L.M., Vasilevskiy, B.B., Djuraev, A.D., Piyanovskiy, G.V., Michailov, V.V., Divaev, F.K., 2011. Atlas of Ore Deposits Models of Uzbekistan. State Committee of Republic of Uzbekistan on Geology and Mineral Resources, Scientific Research Institute of Mineral Resources, Tashkent, pp. 1–100.
Windley, B.F., Alexeiev, D., Xiao, W., Kröner, A., Badarch, G., 2007. Tectonic models for accretion of the Central Asian Orogenic Belt. J. Geol. Soc. 164, 31–47.
Xiao, W., Windley, B.F., Allen, M.B., Han, C., 2013. Paleozoic multiple accretionary and collisional tectonics of the Chinese Tianshan orogenic collage. Gondwana Res. 23, 1316–1341.
Xue, C.J., Duan, S.G., Chai, F.M., 2013. Maimaiti. M., Tuleshiabekov A.X., and Qu W.J., Metallogenetic epoch of the Almalyk porphyry copper ore field, Uzbekistan, and its geological significance. Earth Sci. Front. 20 (2), 197–204 (in Chinese with English abstract).
Xue, C.J., Zhao, X.B., Mo, X.X., Dong, L.H., Gu, X.X., Nurtaev, B., Pak, N., Zhang, Z.C., Wang, X.L., Zu, B., Zhang, G.Z., Feng, B., Liu, J.Y., 2014. Asian Gold Belt in western Tianshan and its dynamic setting, metallogenic control and exploration. Earth Sci. Front. 21 (5), 128–155 (in Chinese with English abstract).
Yakubchuk, A., Cole, A., Seltmann, R., Shatov, V., 2002. Tectonic setting, characteristics, and regional exploration criteria for gold mineralization in the Altaid orogenic collage: the Tien Shan province as a key example. Soc. Econ. Geol. – Spec. Publ. 9, 177–202.

Yakubchuk, A., Degtyarev, K., Maslennikov, V., Wurst, A., Stekhin, A., Lobanov, K., 2012. Tectonomagmatic settings, architecture, and metallogeny of the Central Asian copper province. Soc. Econ. Geol. – Spec. Publ. 16, 403–432.

Yuan, H., Gao, S., Liu, X., Li, H., Günther, D., Wu, F., 2004. Accurate U-Pb age and trace element determinations of zircon by laser ablation-inductively coupled plasma-mass spectrometry. Geostand. Geoanal. Res. 28, 353–370.

Yuan, H., Gao, S., Dai, M., Zong, C., Gunther, D., Fontaine, G., Liu, X., Diwu, C., 2008. Simultaneous determinations of U-Pb age, Hf isotopes and trace element compositions of zircon by excimer laser-ablation quadrupole and multiple-collector ICP-MS. Chem. Geol. 247, 100118.

Zhao, X.B., Xue, C.J., Chi, G.X., Wang, H.G., Qi, T.J., 2014a. Epithermal Au and polymetallic mineralization in the Tulasu Basin, western Tianshan, NW China: potential for the discovery of porphyry Cu Au deposits. Ore Geol. Rev. 60, 76–96.

Zhao, X.B., Xue, C.J., Symons, D.T., Zhang, Z.C., Wang, H.G., 2014b. Microgranular enclaves in island-arc andesites: a possible link between known epithermal Au and potential porphyry Cu–Au deposits in the Tulasu ore cluster, western Tianshan, Xinjiang, China. J. Asian Earth Sci. 85, 210–223.

Zhao, X.B., Xue, C.J., Chi, G.X., Pak, N., Zu, B., 2015. Re–Os pyrite and U-Pb zircon geochronology from the Taldybulak Levoberezhny gold deposit: insight for Cambrian metallogeny of the Kyrgyz northern Tien Shan. Ore Geol. Rev. 67, 78–89.

Zhao, X.B., Xue, C.J., Chi, G.X., Chu, H.X., Li, Z.H., Pak, N., Wang, X.L., Zhang, G.Z., Zu, B., 2017. Multi-stage gold mineralization in the Taldybulak Levoberezhny deposit, Tien Shan, Kyrgyzstan: reply to comment by Boris Trifonov on "Re–Os pyrite and U-Pb zircon geochronology from the Taldybulak Levoberezhny gold deposit: insight for Cambrian metallogeny of the Kyrgyz northern Tien Shan". Ore Geol. Rev. 82, 217–231.